JETP Letters, Vol. 71, No. 12, 2000, pp. 483–485. Translated from Pis'ma v Zhurnal Éksperimental'noĭ i Teoreticheskoĭ Fiziki, Vol. 71, No. 12, 2000, pp. 705–709.

High-Efficiency Zn Isotope Separation in a Photochemical Reaction Induced by Two-Photon Excitation

P. A. Bokhan, V. V. Buchanov, D. É. Zakrevskiĭ, A. Yu. Stepanov, and N. V. Fateev*

Institute of Semiconductor Physics, Siberian Division, Russian Academy of Sciences, pr. Akademika Lavrent'eva 13, Novosibirsk, 630090 Russia

** e-mail: fateev@isp.nsc.ru*

Received April 21, 2000

High-efficiency laser isotope separation was accomplished for zinc atoms in the situation when isotope shifts are much smaller than the Doppler width. The atoms were excited via two-photon absorption of two counterpropagating waves slightly detuned from the intermediate state, so that all "requisite" atoms were excited. The isotope separation results from a photochemical reaction between the selectively excited zinc isotope and the CO_2 molecules. The reaction rate is 3–5 orders of magnitude higher than for the unexcited atoms. The mechanisms of two-photon resonance line broadening are considered both theoretically and experimentally, and the possibilities of the method for obtaining isotopes in quantitative yields are estimated. © *2000 MAIK "Nauka/Interperiodica".*

PACS numbers: 42.62.Fi

Laser isotope separation of mid-periodic-table elements presents difficulties because of small isotopic splitting. The absence of low-lying autoionizing states with large absorption cross sections imposes additional obstacles. In this work, the zinc atom was chosen as an example to accomplish high-efficiency isotope separation in a photochemical reaction induced by two-photon pumping of excited states and, thereby, to overcome these difficulties.

The scheme of low-lying zinc levels is shown in Fig. 1. According to the literature data [1, 2], the isotopic shift of resonance lines for the even isotopes is mainly due to ground-state isotopic splitting. For the intercombination transition $4s^2\,{}^1S_0 - 4p^3P_1^0$ with $\lambda = 0.307$ μm, the splitting of 660 MHz between two neighboring isotopes is one-third of the Doppler halfwidth. As a result, the whole isotopic structure is masked by the Doppler contour, thus hampering laser isotope separation by the AVLIS methods [3].

To accomplish isotope separation, we have used the photochemical reaction of the long-lived ($\tau \cong 10$ μs) $4p^3P^0$ state with the CO_2 molecule:

$$\mathrm{Zn}(4p^3P^0) + \mathrm{CO_2} - \mathrm{ZnO} + \mathrm{CO} + \Delta E\ (1.33\ \mathrm{eV}). \quad (1)$$

The isotopically selective excitation of atoms into the $6s^3S_1$ state was performed by the absorption of two counterpropagating circularly polarized photons with $\lambda_1 = 307.6$ nm and $\lambda_2 = 303.6$ nm (Fig. 1). The energetic proximity of the photons reduces the Doppler broadening to a value of 20 MHz, which is appreciably smaller than the isotopic shifts. Thereupon, the $6s^3S_1$ state decays into the $4p^3P^0$ state through a sequence of spontaneous and induced transitions both via the intermediate $5p^3P^0_{0,1,2}$ and $5s^3S_1$ levels and directly into the cited state (Fig. 1). Inasmuch as the intercombination transitions between the systems of singlet and triplet levels of the Zn atom are exceedingly weak, all atoms occur in the $4p^3P^0$ state because of fast processes (on the time scale shorter than 30 ns) after the two-photon excitation. To prevent the isotopically nonselective direct excitation of the Zn atom by one-photon pumping through the first intercombination transition, the laser

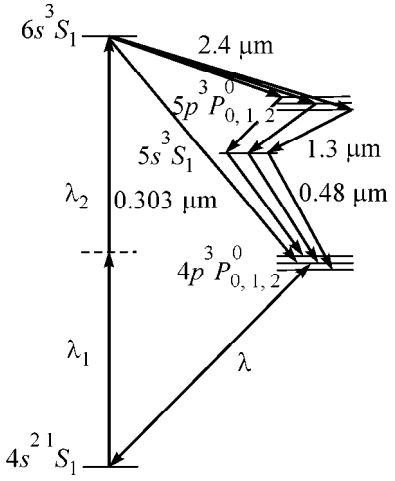

Fig. 1. Scheme of operating levels and transitions in zinc atom.

0021-3640/00/7112-0483$20.00

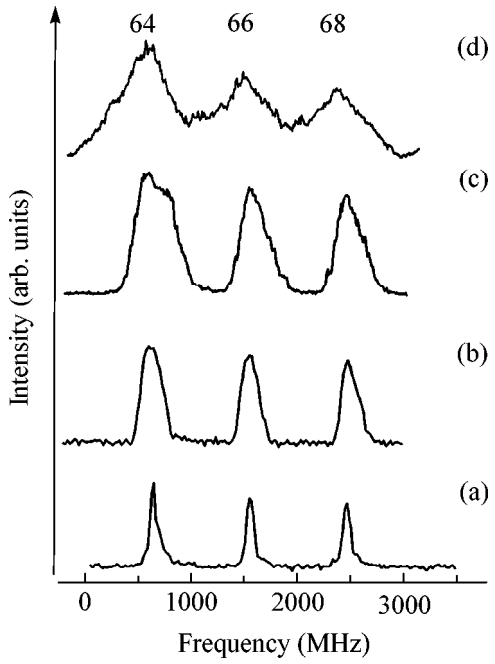

Fig. 2. Luminescence spectrum at a wavelength of 1.3 μm as a function of λ_2: (a) E_1, E_2 = 150 μJ cm^{-2} and $n = 8 \times 10^{-14}$ cm^{-3}; (b) E_1, E_2 = 150 μJ cm^{-2} and $n = 3 \times 10^{-13}$ cm^{-3}; (c) E_1, E_2 = 400 μJ cm^{-2} and $n = 3 \times 10^{-13}$ cm^{-3}; and (d) E_1, E_2 = 550 μJ cm^{-2} and $n = 3 \times 10^{-13}$ cm^{-3}.

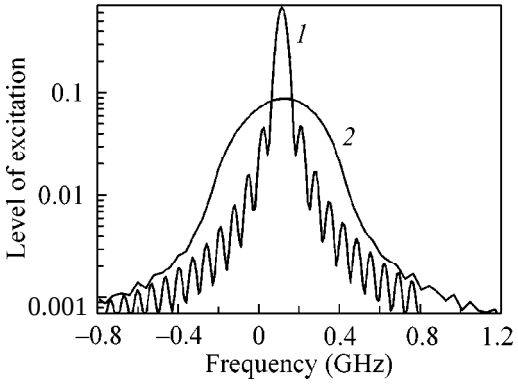

Fig. 3. Frequency dependence of the degree of excitation (*1*) without and (*2*) with allowance made for superradiance. Pulse energy 350 μmJ/cm^2, detuning 7 GHz, and isotope concentration 2×10^{13} cm^{-3}.

frequency was detuned from exact resonance by 4–5 Doppler halfwidths.

Measurements were made on a laser setup containing two identical systems consisting of a driving oscillator and three phenalemine-512 dye amplification stages pumped by a copper vapor laser with an average output of 130 W and pulse repetition rate of 12 kHz. To produce narrow-band emission, a cw rhodamine-6G dye laser pumped by an Ar^+ laser was used as a driving oscillator. The line halfwidth of the driving oscillator was less than 5 MHz. The average output was 10 W for each laser, and the emission line halfwidth was restricted from below by the pulse duration of the Cu laser (≈15 ns). The ultraviolet emission at wavelengths λ_1 = 307.6 nm and λ_2 = 303.6 nm with an average output higher than 2 W was obtained by frequency doubling of the dye lasers in a BBO crystal.

The isotopes were separated in a heated cell blown through with carbon dioxide. The course of reaction (1) was monitored by the appearance of carbon monoxide in the mass spectrum of the output mixture. The rate constants for the background reaction (between the ground-state Zn atoms and the CO_2 molecules) and reaction (1) were measured. In the temperature range 600–800 K, the rate constant for the background reaction is described by the expression

$$K(\text{cm}^3/\text{s}) = 7.9 \times 10^{-8} \exp(-10886/T), \quad T(\text{K}) \quad (2)$$

with an accuracy of no less than 20%. The rate constant for excited-state reaction (1) was monitored by both CO yield and shortening of the $4p^3P_1^0$ lifetime. It was found to be independent, within the measurement error, of the temperature and equal to $k_2 = 2.5 \times 10^{-10}$ cm^3/s, which is 3–5 orders of magnitude (depending on temperature) higher than the rate of the background reaction. At a CO_2 pressure of 15 Pa, the rate of reaction (1) is an order of magnitude higher than the probability of spontaneous decay of the $4p^3P_1^0$ state. The latter, according to our measurements, is equal to $A_c = 10^5$ s^{-1}. Quantum efficiency of the reaction is higher than 50%.

The isotope separation was monitored both by measuring the CO yield in reaction (1) and by the appearance of the optical signal at a wavelength of 1.3 μm in the course of induced transitions (superradiance generation) (Fig. 1). These procedures gave identical spectra for the products of reaction (1). However, because of a considerably higher operation speed, the latter signal is more preferable for electronic locking to the resonant absorption lines and the exclusion of a slow drift of laser frequency in the course of producing the desired isotope.

The luminescence spectra demonstrating Zn isotope separation are shown in Fig. 2. At a low atomic concentration (spectrum a) and a comparatively low laser power, the isotopic structure is completely resolved. The limiting linewidth is equal to 70 MHz for an individual isotope. It is due both to the finiteness of the laser linewidth and to the difference in the photon energies in the two-photon absorption. It is this that is responsible for the asymmetry of the resonances. For a high concentration of Zn atoms (spectrum b) or a high radiation density (spectrum c), the lines of two-photon resonance are strongly broadened and may be completely overlapped (spectrum d).

To obtain a theoretical interpretation of the experimental results and an estimation of the separating power of the method, the level population dynamics were numerically simulated. The radiative lifetimes of the operating levels were found to be longer than the laser pulse duration (5–15 ns). Because of this, the correct estimates can be done only if the processes are considered in the approximation of coherent interaction between radiation and substance. To this end, a computer program was developed for calculating the dynamics of density matrix elements in the three-level scheme according to the mathematical model described in [5]. The model was supplemented by the superradiance-induced transitions from the upper level. The Doppler velocity distribution was also taken into account. The computations were carried out using the Runge–Kutta algorithm of fourth-order accuracy.

An example of the calculated spectral dependence of the degree of excitation of the zinc isotopes is illustrated in Fig. 3. In the absence of superradiance, a sufficiently high degree of isotope excitation (at a level of 0.6) is achieved for a linewidth of about 70 MHz. However, two-photon excitation inevitably brings about population inversion and superradiant transitions between the upper level and the components of the $5p^3P^0_{0,1,2}$ triplet. Since the superradiance line contour entirely covers the Doppler contour, its width is much greater than the inverse pulse duration time. The induced transitions destroy the polarization phases in the two-photon process, also contributing to the broadening of absorption lines (Fig. 2d).

In accordance with the experimental data, the computations show that the absorption line broadens as the concentration of isotope atoms or the emission intensity increases. This effect can be explained by an increase in the fraction of absorbed radiation and ensuing rise in the superradiance power and, hence, the probability of induced transitions. As a result, the absorption line broadens, leading to a decease in the selectivity of isotope separation. For a given selectivity of isotope separation, this effect imposes an upper bound on the laser power and the concentration of the desired isotope. The efficiency of isotope separation is determined by the fraction of radiation absorbed during two-photon pumping. It should be noted that all the "requisite" atoms are involved in the absorption of monochromatic radiation in the course of the two-photon absorption of two counterpropagating waves. The separation selectivity is determined by the degree of overlap between the lines of two-photon resonance. The degree of overlap depends on the frequency detuning, emission energy, and atomic concentration. Insofar as the efficiency and selectivity requirements are contradictory to each other, an optimum balance between the yield, efficiency, and separation selectivity should be chosen separately in each particular case. For instance, for a selectivity of 50–100, the radiant energy densities E_1 and E_2 should not exceed 350 μJ cm^{-2}, while the concentration of zinc atoms should not exceed $n = 2 \times 10^{13}$ cm^{-3}. In these conditions, the equivalent absorption coefficient for the ^{66}Zn isotope is as high as $k_\nu \sim (3–4) \times 10^{-3}$ cm^{-1}, allowing the pumping radiation to be efficiently used with a cell of a moderate length of 150–200 cm. In this case, the setup output is 0.6 g/h.

In summary, it is shown that the use of two-photon excitation in conjunction with a photochemical reaction allows efficient isotope separation in the situation where the resonant transitions of all separated isotopes fall within the Doppler contour. Zinc isotopes are separated in a yield of 0.6 g/h.

We are grateful to G.G. Rakhimov for assistance.

REFERENCES

1. G. F. Hately and T. A. Littleffeld, J. Opt. Soc. Am. **48**, 851 (1958).
2. P. Campbell, J. Billowes, and I. S. Grant, J. Phys. B **30**, 2351 (1997).
3. J. A. Paisner, Appl. Phys. B **46**, 253 (1988).
4. L. S. Vasilenko, V. P. Chebotaev, and A. V. Shishaev, Pis'ma Zh. Éksp. Teor. Fiz. **12**, 161 (1976).
5. S. K. Borisov, M. A. Kuz'mina, and V. A. Mishin, Kvantovaya Élektron. (Moscow) **25**, 695 (1995).

Translated by V. Sakun

JETP Letters, Vol. 71, No. 12, 2000, pp. 486–488. Translated from Pis'ma v Zhurnal Éksperimental'noĭ i Teoreticheskoĭ Fiziki, Vol. 71, No. 12, 2000, pp. 710–713.

Interference Quenching of Light Transmitted through a Monolayer Film of Polymer-Dispersed Nematic Liquid Crystal

A. V. Konkolovich*, V. V. Presnyakov, V. Ya. Zyryanov**, V. A. Loĭko*, and V. F. Shabanov****

** Stepanov Institute of Physics, Belarussian Academy of Sciences, Minsk, 220072 Belarus*
e-mail: sasha@iph.krasn.ru; loiko@dragon.bas-net.by
*** Institute of Physics, Siberian Division, Russian Academy of Sciences, Krasnoyarsk, 660036 Russia*
Received April 28, 2000

A theoretical study of light transmission through a polymer with a monolayer ensemble of bipolar nematic droplets under applied electric film is performed. The possibility of interference quenching of monochromatic coherent light directly transmitted through the film is predicted theoretically and realized in the experiment.

PACS numbers: 78.66.-w; 61.30.-v; 78.20.Bh

The propagation of light in close-packed dispersive media is accompanied by interference phenomena, which should be taken into account in determining the characteristics of the transmitted and scattered light [1]. Theoretical studies of the scattering of coherent monochromatic light by a monolayer [1–3] revealed the possibility of interference quenching of the regular component of directly transmitted light. For the experimental realization of this effect, it is necessary that the parameters of the medium satisfy a number of strict requirements imposed on the size and shape of the scattering particles, their refractive index, and their concentration. The use of monolayer films of polymer-dispersed liquid crystals (PDLC) can simplify the solution of this problem, because one of the parameters of such films (the refractive index) can be varied by applying an electric field. This paper presents theoretical analysis and experimental study of the interference quenching of light transmitted through a monolayer PDLC film with a uniaxially ordered ensemble of bipolar nematic droplets in an external electric field.

For the theoretical analysis, we use the following approximations. The nematic droplets have the form of ellipsoids of revolution flattened in the film plane. The droplets are arranged in the polymer film in such a way that their centers lie in a single plane (a monolayer). The orientation ordering of the director inside the nematic droplets has a bipolar configuration with rigidly fixed poles [4–6]. The symmetry axes of all droplets of the ensemble are oriented in one direction in the layer plane. An electric field applied normally to the layer affects the director configuration in the droplets, leading to changes in their light-scattering properties. We will study the dependence of the transmittance $T = I_t/I_0$ (where I_t and I_0 are the transmitted and incident light intensities, respectively) on the voltage applied to the layer for coherently scattered light in the case of film illumination by normally incident, linearly polarized light with the polarization along the direction of the droplet symmetry axes.

The coherent transmittance T of a monolayer of isotropic particles has the form [1]

$$T = 1 - Q\eta + \frac{Q^2 L}{2}\eta^2, \qquad (1)$$

where Q is the extinction efficiency factor; the parameter L is determined by the amplitude of the scattering function at zero scattering angle; and η is the monolayer filling coefficient (the area fraction of droplets) equal to the ratio of the total area of the projections of all particles (droplets in the case of a PDLC monolayer) onto the monolayer plane to the area over which they are distributed. For a PDLC monolayer characterized by an optical anisotropy of LC droplets, Eq. (1) is retained but the values of Q and L are different in each specific case and determined by the size and shape of the droplets, as well as by their internal structure, depending on the control voltage.

For bipolar nematic droplets with rigidly fixed poles, the refractive index of the extraordinary wave n_e is a function of the control voltage U, and it is calculated according to the procedure proposed in [5, 6]. For the case of incident light with an electric vector oriented along the symmetry axes of the droplets, the anomalous diffraction approach yields the following relationships for the parameters Q and L of a monolayer

with a gamma-distribution of droplets in size:

$$Q = 2\mathrm{Re}K, \tag{2}$$

$$Q^2L/2 = \mathrm{Re}K^2 + \mathrm{Im}K^2. \tag{3}$$

Here, the mean values of the real and imaginary parts, ReK and ImK, of the Hulst function K [7] are determined by the expressions

$$\mathrm{Re}K = 1 + B_e\Bigg[1 - \frac{C_e}{D_e}$$
$$\times \cos\Bigg((\mu+2)\arctan\frac{\nu_m^e}{\mu} - \arctan\frac{\nu_m^e}{\mu}(\mu+2)\Bigg)\Bigg],$$
$$\mathrm{Im}K = \frac{B_eC_e}{D_e} \tag{4}$$
$$\times \sin\Bigg((\mu+2)\arctan\frac{\nu_m^e}{\mu} - \arctan\frac{\nu_m^e}{\mu}(\mu+2)\Bigg),$$

where

$$B_e = \frac{2\mu^2}{(\nu_m^e)^2(\mu+1)(\mu+2)},$$

$$C_e = \left(1 + \frac{(\nu_m^e)^2(\mu+2)^2}{\mu^2}\right)^{1/2}, \quad D_e = \left(1 + \frac{(\nu_m^e)^2}{\mu^2}\right)^{\mu+2},$$

μ is the parameter of the gamma distribution,

$$\nu_m^e = \frac{2\pi\bar{c}n_p}{\lambda}(n_e(U)/n_p - 1), \tag{5}$$

n_p is the refractive index of the polymer, λ is the wavelength of the incident light, and $\bar{c}$ is the mean size of the LC droplets along the normal to the layer.

Theoretical estimates show that, for a PDLC monolayer with a mean droplet size of 12 μm and a variation coefficient of 0.2, interference quenching for a wave with $\lambda = 0.633$ μm occurs when the filling coefficient is $\eta = 0.7$ and the refractive indices are $n_p = 1.52$ and $n_e(U) = 1.56$.

For the experimental studies, we prepared samples of a polyvinylbutyral-dispersed 5CB nematic liquid crystal. The parameters of these samples were close to the calculated values necessary for interference quenching to occur. The liquid crystal was dispersed in the polymer according to the SIPS technique [8]. The uniaxial orientation of the ensemble of nematic droplets was achieved by means of uniaxial tension of the composite film [4]. The thickness of the films studied in the experiment was 16 μm. Figure 1 shows the micrograph of a sample area; the micrograph was obtained with the use of crossed polarizers. The filling coefficient was $\eta = 0.7$. The droplet size $\bar{c}$ varied between 10 and 14 μm with a mean value of 12 μm. The refractive index of the polymer matrix was $n_p = 1.52$. The refractive index of the 5CB liquid crystal was $n_o = 1.53$ for the ordinary wave, and, for the extraordinary wave with the electric vector oriented along the director of the nematic, it was $n_e(\max) = 1.717$ (the values are presented for $\lambda = 0.633$ μm [5, 6]).

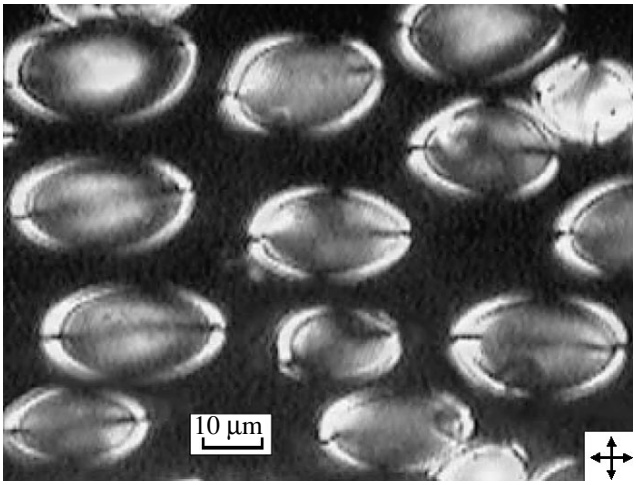

Fig. 1. Micrograph of a PDLC film; the image is obtained by using crossed polarizers whose orientation is shown by the arrows.

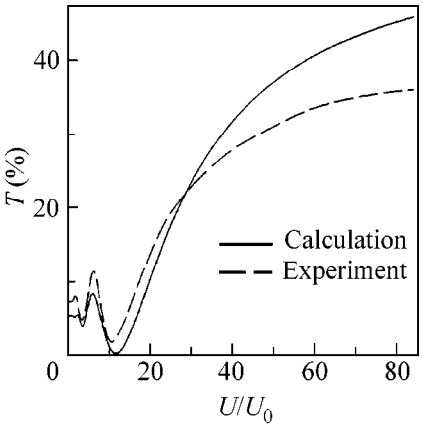

Fig. 2. Calculated and experimental dependences of the transmittance of a PDLC film on the control voltage normalized to the threshold value.

The source of radiation was a He–Ne laser with $\lambda = 0.633$ μm. The intensity of light transmitted through the sample and a circular aperture of diameter 1 mm placed at a distance of 143 cm from the sample was measured by a photodiode operating in a linear mode. The dependence of the intensity of transmitted light on the voltage applied to the sample was recorded by an X–Y plotter.

Figure 2 shows the calculated and measured values of the transmittance of the sample under study versus the control voltage normalized to the threshold value. The oscillatory behavior of the dependence is caused by the oscillations of the extinction efficiency factor Q

as a function of the control voltage. The number of oscillations is determined by the droplet size. One can see that the theoretical and experimental data are in good qualitative agreement.

We note that the minimum observed in the calculated dependence near $U/U_0 = 11.7$ occurs at $QL\eta = 1$ (see Eq. (1)). If, in addition, we have $L = 0.5$, the value of the transmittance T becomes zero; i.e., interference quenching of the directly transmitted light takes place. For the experimental dependence, the minimum value of the transmittance $T = 1.7\%$ is observed at $U/U_0 = 10.8$. The difference between the experimental and theoretical data is caused by the following factors. First, in calculating the filling coefficient of the film that is necessary for quenching to occur, one must proceed from the real droplet size distribution. Second, in a real ensemble of bipolar droplets, the uniaxial orientation of the symmetry axes of droplets is imperfect. In the case of even a slight deviation of the droplet symmetry axes from the preferred direction, the transmitted light will contain an ordinary component for which the conditions of interference quenching are not valid.

Thus, by theoretically analyzing the interference features of the electro-optical response of dispersed nematic liquid crystal monolayers, we arrived at the conclusion that, in PDLC films, quenching of the directly transmitted coherent monochromatic light is possible. According to the theoretical estimates, special samples were prepared on the basis of PDLC monolayers. For these samples, we observed an interference quenching effect that was characterized by a minimum coherent transmittance of 1.7%.

In practical applications, PDLC films with a multilayer droplet arrangement are more common [8]. In this case, one obtains a high contrast due to the multiple scattering of light. Such films are fairly thick (20–30 μm) and hence have a high control voltage. The studies described above open up prospects for the development of thin PDLC monolayers with a high contrast and a low-voltage control.

This work was supported in part by the Ministry of Science and the Ministry of Education of the Russian Federation, by the INTAS (grant no. 97-1923), and by the Krasnoyarsk Science Foundation. The theoretical studies were supported in part by the INCO-Copernicus program (contract no. IC15-CT98-CT98-0806).

REFERENCES

1. A. P. Ivanov, V. A. Loĭko, and V. P. Dik, *Light Propagation in Close-Packed Dispersive Media* (Nauka i Tekhnika, Minsk, 1988).
2. V. A. Loĭko and A. V. Konkolovich, Mol. Cryst. Liq. Cryst. **303**, 41 (1997).
3. V. A. Loĭko and A. V. Konkolovich, Mol. Cryst. Liq. Cryst. **320**, 337 (1998).
4. V. Ya. Zyryanov, V. V. Presnyakov, and V. F. Shabanov, Pis'ma Zh. Tekh. Fiz. **22** (14), 22 (1996) [Tech. Phys. Lett. **22**, 563 (1996)].
5. A. V. Shabanov, V. V. Presnyakov, V. Ya. Zyryanov, and S. Ya. Vetrov, Pis'ma Zh. Éksp. Teor. Fiz. **67**, 696 (1998) [JETP Lett. **67**, 733 (1998)].
6. A. V. Shabanov, V. V. Presnyakov, V. Ya. Zyryanov, and S. Ya. Vetrov, Mol. Cryst. Liq. Cryst. **321**, 245 (1998).
7. H. C. van de Hulst, *Light Scattering by Small Particles* (Wiley, New York, 1957; Inostrannaya Literatura, Moscow, 1961).
8. G. M. Zharkova and A. S. Sonin, *Liquid-Crystal Composites* (Nauka, Novosibirsk, 1994).

Translated by E. Golyamina

JETP Letters, Vol. 71, No. 12, 2000, pp. 489–492. Translated from Pis'ma v Zhurnal Éksperimental'noĭ i Teoreticheskoĭ Fiziki, Vol. 71, No. 12, 2000, pp. 714–719.

Photonic-Crystal Fibers with a Photonic Band Gap Tunable within the Range of 930–1030 nm

M. V. Alfimov*, A. M. Zheltikov, A. A. Ivanov*, V. I. Beloglazov***, B. A. Kirillov**, S. A. Magnitskiĭ**, A. V. Tarasishin**, A. B. Fedotov**, L. A. Mel'nikov****, and N. B. Skibina*****

** Center of Photochemistry, Russian Academy of Sciences, ul. Novatorov 7a, Moscow, 117421 Russia*

*** International Laser Center, Faculty of Physics, Moscow State University, Vorob'evy gory, Moscow, 119899 Russia*

e-mail: zheltikov@top.phys.msu.su

**** Institute of Technology and Processing of Glass Structures, Russian Academy of Sciences, Saratov, 410044 Russia*

***** Saratov State University, Saratov, 410026 Russia*

Received May 18, 2000

The physical principles of photonic-crystal fibers with a photonic band gap tunable in the visible and near-IR spectral ranges are demonstrated. Direct numerical integration of the Maxwell equations with the use of the finite-difference time-domain technique reveals the possibility of creating holey fibers with a photonic-crystal cladding whose photonic band gap lies within the frequency range characteristic of widespread solid-state femtosecond lasers. The fabrication of holey fibers with a pitch of the two-dimensional periodic structure of the cladding less than 500 nm allowed us to experimentally observe a photonic band gap in transmission spectra of holey fibers tunable within the range of 930–1030 nm. This photonic band gap is satisfactorily described within the framework of the proposed numerical approach based on the finite-difference time-domain method. *© 2000 MAIK "Nauka/Interperiodica".*

PACS numbers: 42.70.Qs; 42.81.Qb

The spectral range of single-mode waveguiding in conventional optical fibers is usually not very broad [1]. As the frequency of optical radiation increases, a conventional fiber becomes multimode, while lowering of radiation the frequency leads to the growth in optical losses. Recently developed optical fibers of a new type having a cladding with the structure of a two-dimensional photonic crystal, i.e., a two-dimensional periodic array of closely packed hollow silica fibers, allow the spectral range of single-mode waveguiding to be considerably expanded due to changes in the effective refractive index of the photonic-crystal cladding with variations in the radiation frequency [2–5]. Fibers of this type are of considerable interest, as they allow many important problems of fiber optics to be solved and many ideas of the physics of photonic crystals [6–8] to be implemented in practice. The first experiments devoted to the investigation of the properties of photonic-crystal fibers (also referred to as "holey" fibers) have demonstrated that such fibers support a single-mode propagation regime within a broad spectral range, allowing radiation energy losses to be considerably reduced in this regime [2]. These experiments stimulated intensive investigations into the waveguide properties of holey fibers, which allowed the mode structure of radiation in such fibers to be revealed [3], the boundaries of the single-mode regime to be found [4], and the frequency dependence of laser-radiation divergence to be determined [5]. Holey fibers also hold much promise for nonlinear-optical applications. In particular, the high localization degree of the light field in the core of a holey fiber suggests a way to considerably improve the efficiency of nonlinear-optical interactions in such materials [9]. Recent experiments [10, 11] have shown that these properties of holey fibers can be employed to control the spectra of ultrashort laser pulses and to generate a supercontinuum.

Investigations of the optical properties of holey fibers have been restricted until now to propagation regimes where the radiation wavelength is much less than the pitch of the photonic-crystal cladding and the core diameter. In this regime, the existence of a photonic band gap has, in fact, no influence on the propagation of light in a fiber. The purpose of this paper is to demonstrate the physical principles of holey fibers with a photonic band gap (PBG) of the cladding tunable within the visible and near-IR spectral ranges. By means of direct numerical integration of the Maxwell equations with the use of the finite-difference time-domain (FDTD) technique, we will show that the transmission spectrum of a photonic-crystal cladding in a holey fiber may display a photonic band gap within the frequency range characteristic of the available convenient femtosecond lasers if a two-dimensional periodic structure with a period less than 500 nm is employed as a cladding in such a fiber. We have fabricated and

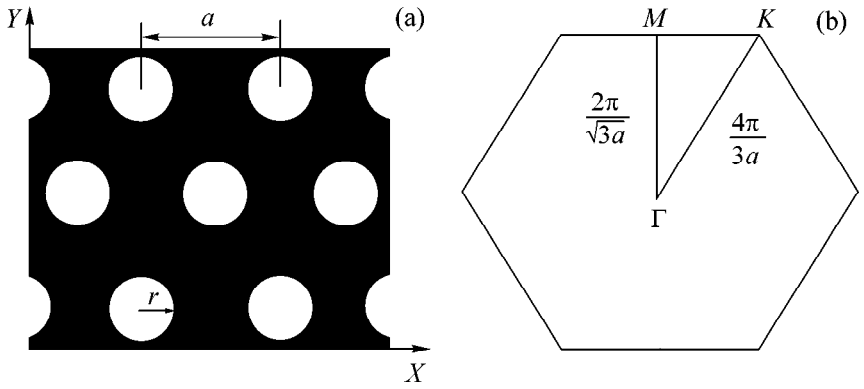

Fig. 1. (a) Triangular lattice of air holes in glass and (b) the corresponding first Brillouin zone of the photonic-crystal cladding of a holey fiber.

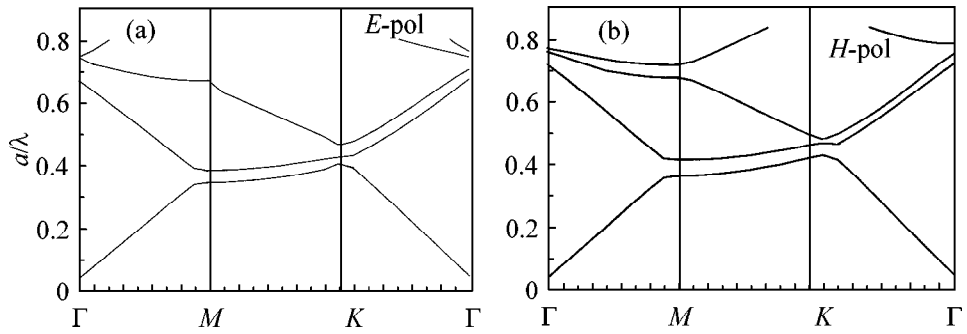

Fig. 2. The band structure of photon energies for (a) *E*- and (b) *H*-polarized radiation fields in a triangular lattice of air holes in glass with $r/a = 0.4$ and $n = 1.5973$.

experimentally studied holey fibers meeting this requirement. Analysis of transmission spectra of these fibers measured in the direction perpendicular to the direction of waveguiding has revealed the existence of a photonic band gap within the wavelength range from 930 to 1030 nm. Our experiments have also demonstrated the possibility of tuning the photonic band gap of the photonic-crystal cladding in holey fibers by filling air holes in the cladding with alcohol.

To calculate the structure of the photonic band gap for a photonic-crystal cladding of holey fibers, we performed direct numerical integration of the Maxwell equations using the FDTD technique [12]. We considered an array of cylindrical air holes with a radius r and an infinite length arranged into a two-dimensional periodic triangular-lattice structure in a glass (Fig. 1a). The first Brillouin zone for such a photonic-crystal lattice has the form of the regular hexagon shown in Fig. 1b.

The details of the FDTD procedure adapted for two-dimensional PBG structures can be found in [13]. In our simulations, we employed periodic boundary conditions, while the initial conditions were taken in the form of a plane wave with wave vectors subject to the boundary conditions. Then, applying the FDTD method to integrate the Maxwell equations and performing the Fourier transform of the field evolution obtained with the use of this procedure for arbitrary points of the simulation area, we were able to find the eigenfrequencies corresponding to the chosen values of the wave vectors. Repeating this procedure for all the wave vectors from the first Brillouin zone, we simulated the band structure of photonic energies and determined the form of the photonic band gap. The above procedure was employed to determine the band structure of photonic energies for a two-dimensional photonic-crystal lattice with $r/a = 0.4$ and $n = 1.5973$. The errors of simulations for PBG structures with such parameters do not exceed 1%. The band structure of photonic energies for *E*- and *H*-polarized radiation fields is presented in Fig. 2. The results of our simulations show that the creation of holey fibers with a photonic band gap lying in the wavelength range characteristic of the available convenient femtosecond titanium sapphire and forsterite lasers requires the fabrication of a two-dimensional PBG fiber structure with a pitch less than 500 nm.

The technology employed to fabricate holey fibers with such parameters was similar to the technology described in [10] and was based on the following procedure. Identical glass capillaries were stacked into a

periodic structure, which was then fused at a high temperature in order to eliminate air gaps between the capillaries, and drawn. The resulting structure was cut into segments. These segments were also stacked into a periodic array, which underwent the drawing process again. These technological stages were repeated until a pitch (the distance between the centers of the air holes) of 32 μm was achieved. At the final stage, a holey fiber with a desirable pitch was obtained by pulling the 32-μm-pitch structure inside a glass shell. The initial inner diameter of the glass capillaries used in this process was about 1 mm. The above procedure allowed us to fabricate fibers where the cladding had a structure of a two-dimensional photonic crystal with several hundred periodically arranged air holes. Special precautions were taken to keep the annular shape of the air holes and to eliminate the air gaps between the neighboring capillaries. Two-dimensional photonic crystals with a period of the PBG structure less than 0.5 μm and a ratio of the diameter of the air holes to the pitch of the structure equal to 0.4 were fabricated with the use of this technology. An image of such a PBG structure obtained with the use of a scanning electron microscope is shown in Fig. 3. A defect was introduced into this two-dimensional photonic-crystal structure by replacing the central capillary by a usual fiber made of glass of another type. This central fiber served as the core in a PBG waveguide.

The periodic structure in the cladding of a holey fiber gives rise to photonic band gaps in the transmission spectrum of the structure measured in the direction perpendicular to the direction of waveguiding. Two-dimensional periodic structures with a period less than 500 nm allowed us to observe photonic band gaps within the wavelength range characteristic of widespread lasers. The experimental setup for measuring the spectra of holey fibers was based on a Hitachi-333 spectrophotometer and included the signal and reference channels. A 5-cm-focal-length quartz lens was used in the signal channel to ensure the predominant illumination of the central part of a sample having a photonic-crystal structure. This lens focused the light beam on a slit diaphragm with an aperture $d = 150$ μm. A holey-fiber sample was placed behind the diaphragm. Radiation transmitted through the sample was collimated with a quartz lens, which was identical to the focusing lens. Transmission spectra were measured within the range of wavelengths from 400 to 1400 nm. To be able to measure transmission spectra of a photonic-crystal sample for different directions of the wave vector in the first Brillouin zone of the photonic-crystal lattice, we rotated the sample around its axis corresponding to the direction of waveguiding.

Transmission spectra measured for a holey fiber with a period of the PBG structure less than 500 nm are presented in Fig. 4. The photonic band gap in the transmission spectra of such samples was observed within the range of wavelengths from 930 to 1030 nm. Since air holes periodically arranged in the fiber cladding form a hexagonal lattice, the position of the photonic band gap in the transmission spectrum changes, depending on the rotation angle of the structure with respect to incident radiation. Comparison of the results of simulations and experimental data (Figs. 3, 4) shows that the position of the photonic band gap can be satisfactorily described within the framework of the numerical approach based on the direct integration of the Maxwell equations with the use of the FDTD technique.

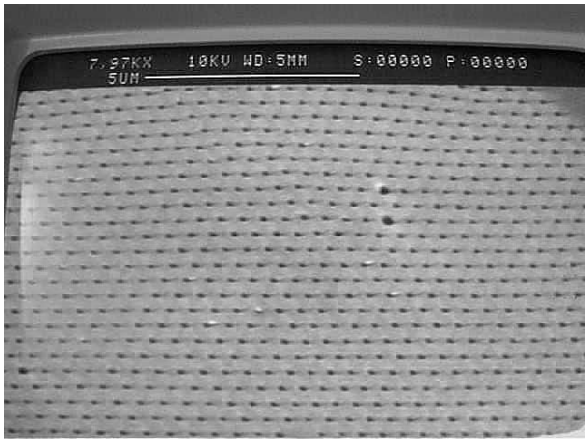

Fig. 3. Scanning electron microscope image of the photonic-crystal cladding in a holey fiber. The horizontal bar at the top of the figure corresponds to a distance of 5 μm.

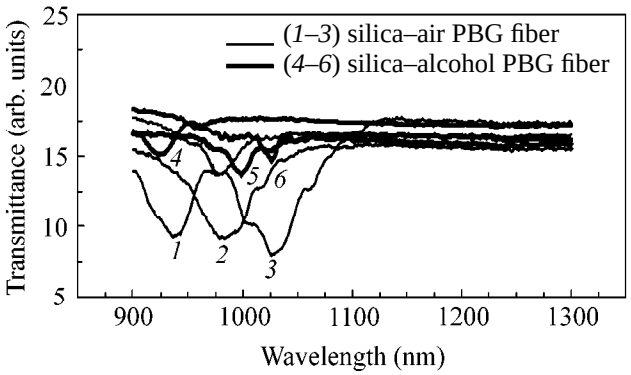

Fig. 4. Transmission spectra of a photonic-crystal fiber measured for different directions of the wave vector in the first Brillouin zone of the photonic-crystal lattice of the PBG cladding for (*1–3*) silica–air and (*4–6*) silica–alcohol PBG structures.

The structure of the photonic band gap in the transmission spectrum of a photonic-crystal structure depends on the ratio of the refractive indices of the materials forming the structure. In the case of holey fibers, this circumstance opens up the opportunity of tuning the photonic band gap by filling the air holes in the PBG structure with various materials whose refractive indices differ from unity.

We have studied changes in the photonic band gap of holey-fiber samples arising when the air holes of the structure were filled with alcohol. As can be seen from the results presented in Fig. 4 (curves *4–6*), the position and the width of the photonic band gap noticeably change in this case.

Thus, direct numerical integration of the Maxwell equations with the use of the finite-difference time-domain technique reveals the possibility of creating holey fibers with a photonic-crystal cladding whose photonic band gap lies within the frequency range characteristic of the available convenient femtosecond titanium sapphire and forsterite lasers if a two-dimensional periodic structure with a period less than 500 nm is employed as a cladding in such fibers. The fabrication of holey fibers meeting this requirement allowed us to experimentally demonstrate the existence of a photonic band gap for such structures within the range of 930–1030 nm by measuring the transmission spectra of holey fibers in the direction perpendicular to the direction of waveguiding. This photonic band gap is satisfactorily described within the framework of a numerical approach based on direct integration of the Maxwell equations with the use of the FDTD technique. The experimentally demonstrated possibility of tuning the photonic band gap of a photonic-crystal cladding in holey fibers by using various materials to fill the air holes in the fiber cladding offers broad opportunities for tuning the dispersion of holey fibers and controlling the luminescence of molecules within a broad spectral range.

This study was supported in part by the President of Russian Federation Grant no. 00-15-99304, the Russian Foundation for Basic Research (project no. 00-02-17567), and INTAS (grant no. 97-0369).

REFERENCES

1. A. W. Snyder and J. D. Love, *Optical Waveguide Theory* (Chapman and Hall, New York, 1983).
2. J. C. Knight, T. A. Birks, P. St. J. Russell, and D. M. Atkin, Opt. Lett. **21**, 1547 (1996).
3. J. C. Knight, T. A. Birks, R. F. Cregan, *et al.*, Opt. Mater. **11**, 143 (1999).
4. T. A. Birks, J. C. Knight, and P. St. J. Russell, Opt. Lett. **22**, 961 (1997).
5. M. J. Gander, R. McBride, J. D. C. Jones, *et al.*, Opt. Lett. **24**, 1017 (1999).
6. E. Yablonovitch, J. Opt. Soc. Am. B **10**, 283 (1993).
7. J. Joannopoulos, R. Meade, and J. Winn, *Photonic Crystals* (Princeton Univ., Princeton, 1995).
8. N. I. Koroteev, S. A. Magnitskii, A. V. Tarasishin, and A. M. Zheltikov, Opt. Commun. **159**, 191 (1999).
9. N. G. R. Broderick, T. M. Monro, P. J. Bennett, and D. J. Richardson, Opt. Lett. **24**, 1395 (1999).
10. A. B. Fedotov, A. M. Zheltikov, L. A. Mel'nikov, *et al.*, Pis'ma Zh. Éksp. Teor. Fiz. **71**, 407 (2000) [JETP Lett. **71**, 281 (2000)].
11. J. K. Ranka, R. S. Windeler, and A. J. Stentz, Opt. Lett. **25**, 25 (2000).
12. A. Taflove, *Computational Electrodynamics: The Finite-Difference Time-Domain Method* (Artech House, Norwood, 1995).
13. A. M. Zheltikov, S. A. Magnitskiĭ, and A. V. Tarasishin, Zh. Éksp. Teor. Fiz. **117**, 691 (2000) [JETP **90**, 600 (2000)].

Translated by A. Zheltikov

JETP Letters, Vol. 71, No. 12, 2000, pp. 493–495. Translated from Pis'ma v Zhurnal Éksperimental'noĭ i Teoreticheskoĭ Fiziki, Vol. 71, No. 12, 2000, pp. 720–723.

Isotope Effect in (La-Pr-Ca)MnO_3 Manganites

N. M. Plakida

Joint Institute for Nuclear Research, Dubna, Moscow region, 141980 Russia
e-mail: plakida@thsun1.jinr.ru
Received May 18, 2000

An explanation of the "giant" oxygen isotope effect is suggested for the Curie temperature T_C of the $(La_{0.75}Pr_{0.25})_{0.7}Ca_{0.3}MnO_3$ compound. The model takes into account the proximity of the ferromagnetic transition to the dielectric antiferromagnetic phase. To explain the experimental data, it is sufficient to include a weak electron–phonon interaction for free charge carriers. © *2000 MAIK "Nauka/Interperiodica".*

PACS numbers: 75.30.Kz; 71.38.+i

In recent experiments [1], the "giant" isotope effect was discovered for the Curie temperature T_C of the $(La_{1-y}Re_y)_{1-\delta}Ca_\delta MnO_3$ (Re = Nd and Pr) compounds. In particular, the isotope substitution of oxygen ^{18}O for ^{16}O fully suppressed the ferromagnetic (FM) transition in the $(La_{0.5}Nd_{0.5})_{0.67}Ca_{0.33}MnO_3$ [2] and $(La_{0.25}Pr_{0.75})_{0.7}Ca_{0.3}MnO_3$ (LPCM-0.75) [3, 4] compounds and the ensuing transition from the semiconductor to the metal phase. With the aim of revealing the nature of the giant isotope effect, a partial isotope substitution ($^{16}O_{1-x}{}^{18}O_x$) in the LPCM-0.75 compound was carried out in [5, 6]. Neutron diffraction studies [5] showed that Curie temperature T_C of the FM transition linearly decreased with increasing concentration x of the ^{18}O isotope:

$$T_C(x) \simeq T_C^0(1 - ax), \quad x \le 0.6,$$
$$T_C^0 \simeq 120 \text{ K}, \quad a \simeq 0.56, \tag{1}$$

while the conductivity measurements showed a linear decrease in the temperature T_{IM} of transition to the metal phase [6]:

$$T_{IM}(x) \simeq T_{IM}^0(1 - bx), \quad x \le 0.4,$$
$$T_{IM}^0 \simeq 88 \text{ K}, \quad b \simeq 1.1. \tag{2}$$

These experiments provide evidence for the important role of the electron–phonon interaction of the delocalized e_g electrons, responsible for the transition to the ferromagnetic conducting phase, with the oxygen lattice vibrations, among which either the breathing or the Jahn–Teller modes are usually assumed to dominate (see review [7]). However, in attempting to rationalize the giant isotope effect for T_C in these compounds in terms of the commonly accepted double exchange theory (see, e.g., review [8]) with inclusion of polaron formation and ensuing mobile-carrier band narrowing [1, 9],

$$T_C \simeq A\tilde{t} = At\exp(-g^2), \tag{3}$$

one is forced to assume that the coupling is so strong that the polarons are fully localized. In Eq. (3), t is the hopping matrix element for the mobile e_g electrons, and the electron–phonon coupling constant $g^2 \simeq \lambda E_p/\hbar\omega_0 = \gamma\sqrt{M}$ is determined by the polaron energy E_p and the frequency $\omega_0 \propto 1/\sqrt{M}$ of the respective phonon (the constant $\lambda \le 1$ depends on the magnitude of the electron–phonon interaction) [10]. Indeed, according to Eq. (3),

$$\Delta T_C/T_C \simeq \Delta\tilde{t}/\tilde{t}$$
$$= \exp\{g^2(1 - \sqrt{18/16})\} - 1 \simeq -0.06g^2, \tag{4}$$

so that the observed shift $\Delta T_C/T_C \simeq 0.56$ [Eq. (1)] of the Curie temperature can only be obtained with a g^2 value as large as 9.4.

In this connection, it was hypothesized in [4] that the Curie temperature is close to the charge-ordering temperature T_{co} in the compounds with high Pr concentration such as LPCM-0.75. Indeed, recent experiments [11–13] showed that, on lowering the temperature, the LPCM-y compounds with high Pr content ($y > 0.6$) first undergo the transition to the charge-ordered antiferromagnetic (AFM) phase, whereupon a large-hysteresis first-order transition to the FM phase occurs. This indicates the proximity of the AFM and FM phases.

In this work, we take into account the experimentally observed proximity of the FM and AFM transitions to suggest that the Curie temperature is determined by the competition between the double exchange of e_g electrons and the indirect AFM exchange J_{AF} of the t_{2g} electrons:

$$T_C = A(\tilde{t} - t_c^F) = A\tilde{t}(1 - t_c^F/\tilde{t}), \tag{5}$$

where $t_c^F \propto J_{AF}$. As a theoretical substantiation of this model, noteworthy are the phase diagram calculations within the framework of the double exchange model including the orbital degeneracy of the e_g electrons, their Coulomb repulsion, and the indirect AFM exchange J_{AF} of the localized t_{2g} electrons having a total spin of 3/2 [14]. It was shown in these calculations that at large J_{AF} values ($J_{AF}/t \geq 0.04$ for zero temperature and carrier concentration of 0.5), the first-order phase transition occurs from the FM to the AFM phase. It is worth noting recent work [15], where the double-exchange model with the inclusion of indirect AFM exchange was used in the finite-cluster Monte Carlo calculations to demonstrate that the FM transition is linearly suppressed with a rise in J_{AF}.

Model (5) incorporates three independent parameters: At, g^2, and t_c^F/t. Two of them can be derived from the data on T_C and ΔT_C:

$$\frac{\Delta T_C}{T_C} = \frac{\Delta\tilde{t}/\tilde{t}}{1 - t_c^F/\tilde{t}} = -\frac{0.06g^2}{1 - t_c^F/\tilde{t}}. \quad (6)$$

The third parameter calls for theoretical estimates. With the double-exchange model, one has in Eq. (3) for manganites: $At \simeq z\delta t$, where $t \simeq 0.2$ eV is the hopping matrix element, $z = 6$ is the number of nearest neighbors, and $\delta = 1 - n$ is the concentration of hole carriers (see, e.g., [16]).

Let us consider the LPCM-0.75 compound with $\delta = 0.3$. For the ^{16}O composition, a decrease in temperature first initiates the transition to the charge-ordered phase at $T_{co} \simeq 180$ K and thereafter, the transition to the AFM phase at $T_N \simeq 150$ K and to the FM phase at $T_C(x = 0) \simeq 120$ K [12, 13]. Consequently, one obtains from the T_C/At ratio $\exp(-g^2) - t_c^F/t = T_C/At \simeq 0.03$. The smallness of this parameter (because of the proximity of the transition to the AFM phase) allows one to naturally explain the appreciable lowering of T_C compared to its value $T_C^0 = At \simeq 4000$ K in the double-exchange model [16]. To estimate the dependence of the hopping matrix element on the concentration of $^{18}O_x$ isotope upon a partial isotope substitution, let us use the simplest mean-field approximation

$$\tilde{t}(x) = \tilde{t}_{16}(1 - x) + \tilde{t}_{18}x = \tilde{t} + x\Delta\tilde{t}, \quad (7)$$

where $\tilde{t} = \tilde{t}_{16}$, $\Delta\tilde{t} = \tilde{t}_{18} - \tilde{t}_{16}$, and $\tilde{t}_{16(18)}$ are the hopping matrix elements for the Mn–O–Mn bond containing oxygen $^{16(18)}$O. According to Eqs. (5) and (7), this approximation (with respect to $1/z$) gives the experimentally observed linear dependence $T_C(x)$ and, hence, is adequate. Comparing this dependence with Eq. (1), one arrives at the following equation for the polaron reduction constant: $g^2\exp(-g^2) \simeq 0.27$; i.e., $g^2 \simeq 0.4$. One can see that, indeed, the giant isotopic shift $\Delta T_C/T_C \simeq -0.56$ [the isotopic index $\alpha_O = -(\Delta T_C/T_C)/(\Delta M/M) \simeq 4.5$] can be explained within the framework of the suggested model even if the electron–phonon coupling is weak.

In conclusion, let us make a few general remarks. An alternative explanation of the isotope effect was given in [17], invoking the dynamic Jahn–Teller effect, according to which the oxygen ions move in a two-well potential and the hopping matrix element for the delocalized e_g electrons is strongly reduced: $t \simeq t_0F$, where $F = \exp(-\kappa^2)$. This model also encounters certain difficulties in the explanation of the giant isotope effect, because the κ^2 parameter should be anomalously large.

The model suggested in this work can be used for an analysis of the isotope effect for the T_{co} temperature of transition to the charge-ordered state. As shown in [14], the latter occurs in the presence of Coulomb repulsion V of the e_g electrons and can occur in both AFM and FM phases if the V/t ratio exceeds a certain critical value. For this reason, the polaron renormalization $\tilde{t} = t\exp(-g^2)$ will bring about the isotope effect for the T_{co} temperature as well (see, e.g., [9, 18]). Contrary to the FM transition, the charge-ordering temperature decreases with an increase in the band width (decrease in the V/t ratio) and can be written as

$$T_{co} = B(t_c^{co} - \tilde{t}) = B\tilde{t}(t_c^{co}/\tilde{t} - 1), \quad (8)$$

where $t_c^{co} \propto V$. The analyses of the concentration dependences of T_{co} and (positive) isotope shift $\Delta T_{co}/T_{co}$ can be carried out as above.

In this work, we do not allow for the experimentally observed FM and AFM phase separation near the point of their coexistence (see, e.g., [19]) in LPCM-y at high Pr concentrations [5, 6]. However, neutron diffraction suggests [13] that the dimensions of the FM and AFM phases are large enough for them to be considered as macroscopic objects.

It is also worth noting that the magnetic-field effect on the FM transition (and on the isotope effects for T_C and T_{co}) can be described by the suggested model if the hopping matrix element $t\left(\cos\frac{1}{2}\theta_{ij}\right)$ is taken to be dependent, as in the standard double-exchange model, on the angle θ_{ij} between spins $S = 3/2$ at the neighboring lattice sites (i, j), because this angle changes under the action of an external magnetic field.

Although the suggested model (5) is phenomenological in character, it is based on the inclusion of the interaction between two electron subsystems, viz., the delocalized e_g and the localized t_{2g} electrons typical of manganites. The former are responsible for the FM ordering, and the latter, for the AFM order, as confirmed by numerous microscopic calculations. A more rigorous theoretical substantiation of the model will be

made in a separate work generalizing the calculations [14] to nonzero temperatures and an arbitrary concentration of carriers. As of now, it seems to be difficult to suggest any other explanation for the giant isotope effect observed in recent works [2–6].

I am grateful to A.M. Balagurov and N.A. Babushkina for providing with the experimental results before publication. I also thank K.I. Kugel' and D.I. Khomskiĭ for helpful discussions. This work was supported in part by the INTAS, grant nos. 97-0963 and 97-11066.

REFERENCES

1. G. M. Zhao, K. Conder, H. Keller, *et al.*, Nature (London) **381**, 676 (1996).
2. G. M. Zhao, H. Keller, J. Hoffer, *et al.*, Solid State Commun. **104**, 57 (1997).
3. N. A. Babushkina, L. M. Belova, O. Yu. Gordenko, *et al.*, Nature (London) **391**, 159 (1998).
4. N. A. Babushkina, L. M. Belova, V. I. Ozhogin, *et al.*, J. Appl. Phys. **83**, 7369 (1998).
5. A. M. Balagurov, V. Yu. Pomyakushin, D. V. Sheptyakov, *et al.* (unpublished).
6. N. A. Babushkina, L. M. Belova, A. N. Taldenkov, *et al.* (unpublished).
7. A. J. Millis, Nature (London) **392**, 147 (1998).
8. D. I. Khomskii and G. A. Sawatsky, Solid State Commun. **102**, 87 (1997).
9. Unjong Yu, Yu. V. Skrypnik, and B. I. Min, Phys. Rev. B **61**, 8936 (2000).
10. N. S. Alexandrov and N. F. Mott, Int. J. Mod. Phys. B **8**, 2075 (1994).
11. H. Y. Hwang, S-W. Cheong, P. G. Radaelli, *et al.*, Phys. Rev. Lett. **75**, 914 (1995).
12. A. M. Balagurov, V. Yu. Pomyakushin, D. V. Sheptyakov, *et al.*, Phys. Rev. B **60**, 383 (1999).
13. A. M. Balagurov, P. Fisher, V. Yu. Pomyakushin, *et al.*, Physica B (Amsterdam) **276**–**278**, 536 (2000).
14. G. Jackeli, N. B. Perkins, and N. M. Plakida, Phys. Rev. B **62** (1) (2000) (in press); cond-mat/9910391.
15. Hongsuk Yi, Jaejun Yu, and Sung-Ik Lee, Phys. Rev. B **61**, 428 (2000).
16. K. Kubo and A. Ohata, J. Phys. Soc. Jpn. **33**, 21 (1972).
17. V. Z. Kresin and S. A. Wolf, Philos. Mag. B **76**, 241 (1997); J. Appl. Phys. **83**, 7357 (1998).
18. M. Medarde, P. Lacorre, K. Conder, *et al.*, Phys. Rev. Lett. **80**, 2397 (1998).
19. A. Moreo, S. Yunoki, and E. Dagotto, Science (Washington, D. C.) **283**, 2034 (1999).

Translated by V. Sakun

JETP Letters, Vol. 71, No. 12, 2000, pp. 496–499. From Pis'ma v Zhurnal Éksperimental'noĭ i Teoreticheskoĭ Fiziki, Vol. 71, No. 12, 2000, pp. 724–729.

Opening an Energy Gap in an Electron Double Layer System at the Integer Filling Factor in a Tilted Magnetic Field[1]

E. V. Deviatov, V. S. Khrapaĭ, A. A. Shashkin, V. T. Dolgopolov, F. Hastreiter*, A. Wixforth*, K. L. Campman, and A. C. Gossard****

Institute of Solid State Physics, Russian Academy of Sciences, Chernogolovka, Moscow region, 142432 Russia
e-mail: shashkin@issp.ac.ru
** Ludwig-Maximilians-Universität, D-80539 München, Germany*
*** Materials Department and Center for Quantized Electronic Structures, University of California, 93106 Santa Barbara, California, USA*

Received May 18, 2000; in final form, May 23, 2000

We employ magnetocapacitance measurements to study the spectrum of a double layer system with gate-voltage-tuned electron density distributions in tilted magnetic fields. For the dissipative state in normal magnetic fields at filling factor $\nu = 3$ and 4, a parallel magnetic field component is found to give rise to the opening of a gap at the Fermi level. We account for the effect in terms of parallel-field-caused orthogonality breaking of the Landau wave functions with different quantum numbers for two subbands. *© 2000 MAIK "Nauka/Interperiodica".*

PACS numbers: 72.20.My; 73.40.Kp

Much interest in electron double layers is attracted by their many-body properties in a quantizing magnetic field. These include the fractional quantum Hall effect at filling factor $\nu = 1/2$ [1], the many-body quantum Hall plateau at $\nu = 1$ [2], broken-symmetry states at fractional fillings [3], the canted antiferromagnetic state at $\nu = 2$ [4], etc. Still, the single-electron properties of double layer systems that can be interpreted without appealing to exchange and correlation effects are no less intriguing. A standard double layer with an interlayer distance of about the Bohr radius is a soft two-subband system, if brought into the imbalance regime in which the electron density distribution is two asymmetric maxima corresponding to two electron layers. In such a system, a small interlayer charge transfer significantly shifts the Landau level sets' positions; in particular, the transfer of all electrons into a single quantum level would lead to a shift as large as the cyclotron energy. In a double layer system with gate-bias-controllable electron density distributions at normal magnetic fields, peculiarities were observed in the Landau level fan chart: at fixed integer filling factor $\nu > 2$, the Landau levels for two electron subbands pin to the Fermi level over wide regions of a magnetic field, giving rise to a zero activation energy for the conductivity [5, 6]. The pinning effect is obviously possible due to the orthogonality of the Landau level wave functions with different index and, therefore, it might disappear if the orthogonality were lost for some reason. In contrast, at $\nu = 1$ and 2, the gap was found to be similar to the symmetric–antisymmetric splitting at balance and having a finite value for any field. This was explained by subband wave function reconstruction in the growth direction [6].

Here, we study the electron spectrum of a gate-voltage-tunable double layer in tilted magnetic fields. We find that for the dissipative state at filling factor $\nu = 3$ and 4 in a normal magnetic field, the addition of a parallel field component leads to the appearance of a gap at the Fermi level, as indicated by activated conductivity. These findings are explained in terms of a wave-function orthogonality-breaking effect caused by the parallel magnetic field component.

The samples are grown by molecular beam epitaxy on a semi-insulating GaAs substrate. The active layers form a 760-Å-wide parabolic well. In the center of the well, a 3-monolayer-thick $Al_xGa_{1-x}As$ ($x = 0.3$) sheet is grown, which serves as a tunnel barrier between both parts on either side. The symmetrically doped well is capped by 600-Å AlGaAs and 40-Å GaAs layers. The symmetric–antisymmetric splitting in the bilayer electron system, as determined from far-infrared measurements and model calculations [7], is equal to $\Delta_{SAS} = 1.3$ meV. The sample has ohmic contacts (each of them is connected to both electron systems in two parts of the well) and two gates on the crystal surface with areas 120×120 and 220×120 μm^2. The gate electrode enables us to tune the carrier density in the well, which is equal to 4.2×10^{11} cm^{-2} at zero gate bias, and simultaneously measure the capacitance between the gate and the well. For the capacitance measurements, we additionally apply a small ac voltage $V_{ac} = 2.4$ mV at frequencies in the range 3–600 Hz between the well

[1] This article was submitted by the authors in English.

and the gate and measure both current components as a function of gate bias V_g in normal and tilted magnetic fields in the temperature interval between 30 mK and 1.2 K. An example of the imaginary current component is depicted in Fig. 1; also shown in the inset is the calculated behavior of the conduction band bottom for our sample.

The employed experimental technique is similar to magnetotransport measurements in Corbino geometry: in the low frequency limit, the active component of the current is inversely proportional to the dissipative conductivity σ_{xx}, while the imaginary current component reflects the thermodynamic density of states in a double layer system. Activation energy at the minima of σ_{xx} for integer ν is determined from the temperature dependence of the corresponding peaks in the active current component.

The positions of the σ_{xx} minimum for $\nu = 2$, 3, and 4 in the $(B_\perp, V_g)$ plane are shown in Fig. 2 for both normal and tilted magnetic fields. At the gate voltages $V_{th1} < V_g < V_{th2}$, at which one subband E_1 of the substrate side part of the well is filled with electrons, the experimental points fall onto straight lines with slopes defined by the capacitance between the gate and the bottom electron layer. Above V_{th2}, where a second subband E_2 collects electrons in the front part of the well, a minimum in σ_{xx} at integer ν corresponds to a gap in the spectrum of the bilayer electron system. In this case, the slope is inversely proportional to the capacitance between the gate and the top electron layer. Additional minima of the imaginary current component that are related solely to the thermodynamic density of states in the second subband are shown in Fig. 2 by dashed lines. Hence, each of the two different kinds of minima forms its own Landau level fan chart. In the perpendicular magnetic field, wide disruptions of the fan line at $\nu = 4$ and termination of the line at $\nu = 3$ indicate the absence of a minimum in σ_{xx} (Fig. 2a). As mentioned above, this results from a Fermi-level pinning of the Landau levels for two subbands.

Remarkably, switching on a parallel magnetic field is found to promote the formation of a σ_{xx} minimum at integer $\nu > 2$, particularly at $\nu = 3$ and 4; see Fig. 2b. This implies that the parallel magnetic field suppresses the pinning effect, giving rise to the opening of a gap at the Fermi level in the double layer system.

Figure 3 represents the behavior of the activation energy E_a along the $\nu = 3$ and 4 fan lines in Fig. 2 for different tilt angles Θ of the magnetic field. As seen from Fig. 3a, for filling factor $\nu = 4$ in the normal field, the value of E_a is largest both at the bilayer onset V_{th2} and at balance. In between these it zeroes, which is in agreement with the disappearance of the minimum of σ_{xx} in the magnetic field range between 2.6 and 3.4 T; in the close vicinity of $B = 3$ T, E_a is unmeasurably small, but likely finite, as can be reconciled with the observed σ_{xx} minimum at the fan crossing point of $\nu =$

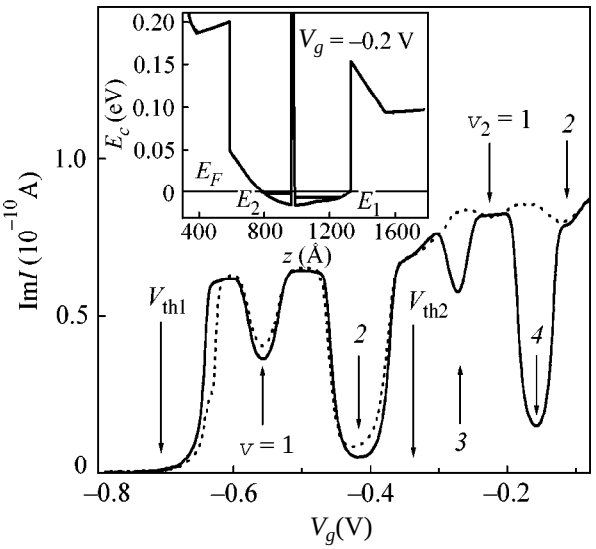

Fig. 1. Dependence of the imaginary current component on gate voltage at a frequency of 100 Hz and temperature of 30 mK for a normal (dashed line) and a tilted by $\Theta = 30°$ (solid line) magnetic field corresponding to the same $B_\perp = 3.3$ T. The filling factors in the whole electron system and in the second subband are indicated. The threshold voltages are determined from Fig. 2 taking account of insignificant threshold shifts in different coolings of the sample. Inset: calculated band diagram of the sample at $V_g = -0.2$ V. Two electron subbands E_1 and E_2 in the quantum well are filled. The coordinate z is counted from the gate.

4 and $\nu_2 = 1$ (Fig. 2a). In contrast, for tilted magnetic fields, the activation energy at $\nu = 4$ never tends to zero, forming a plateau instead (Fig. 3a).

For $\nu = 3$, the parallel field effects are basically similar to the case of $\nu = 4$ with one noteworthy distinction. Near the balance point, the activation energy in a tilted magnetic field exhibits a minimum that deepens with increasing tilt angle, see Fig. 3b. This minimum is likely to be of many-body origin: at sufficiently large Θ it is accompanied by a splitting of the $\nu = 3$ fan line, which is very similar to the behavior of the double layer at $\nu = 2$ discussed as a manifestation of the canted antiferromagnetic phase [4]. This effect will be considered in detail elsewhere.

We relate the appearance of a gap at integer $\nu > 2$ in the unbalanced double layer in tilted magnetic fields to orthogonality breaking of the Landau wave functions with different quantum numbers for two subbands. Indeed, interlayer tunneling should occur with in-plane momentum conservation, so that in a tilted magnetic field it is accompanied with an in-plane shift [8] of the center of the Landau wave function by an amount $d_0 \tan\Theta$, where d_0 is the distance between the centers of mass for electron density distributions in the two lowest subbands. Apparently, the thus-shifted Landau wave functions with different quantum numbers for two subbands become overlapped. In this case, the above-men-

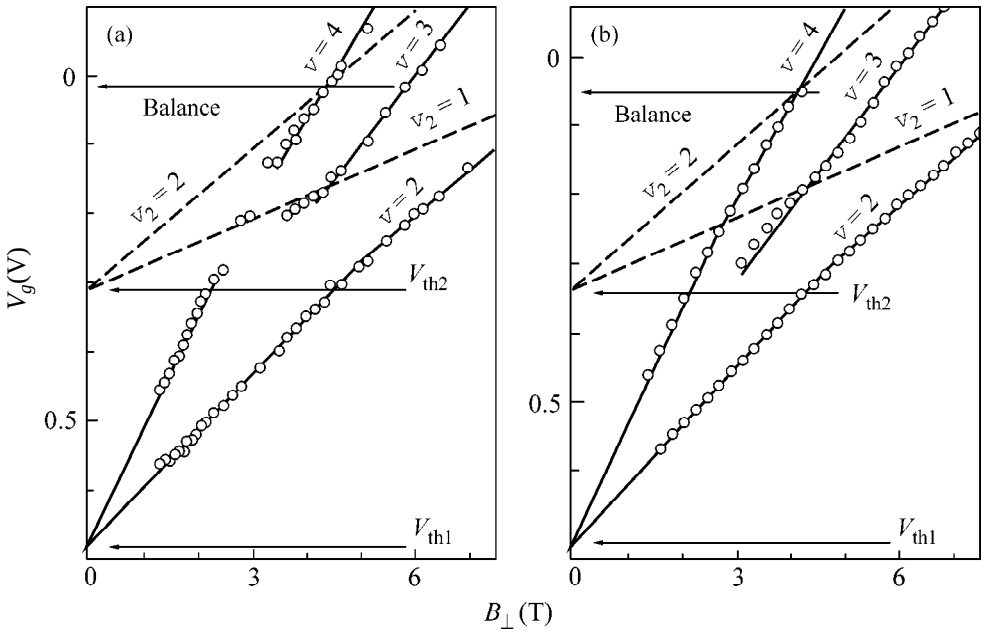

Fig. 2. Positions of the σ_{xx} minima at a temperature of 30 mK for different tilt angles: (a) $\Theta = 0°$, (b) $\Theta = 30°$. The dashed lines correspond to minima in the thermodynamic density of states for the second electron subband.

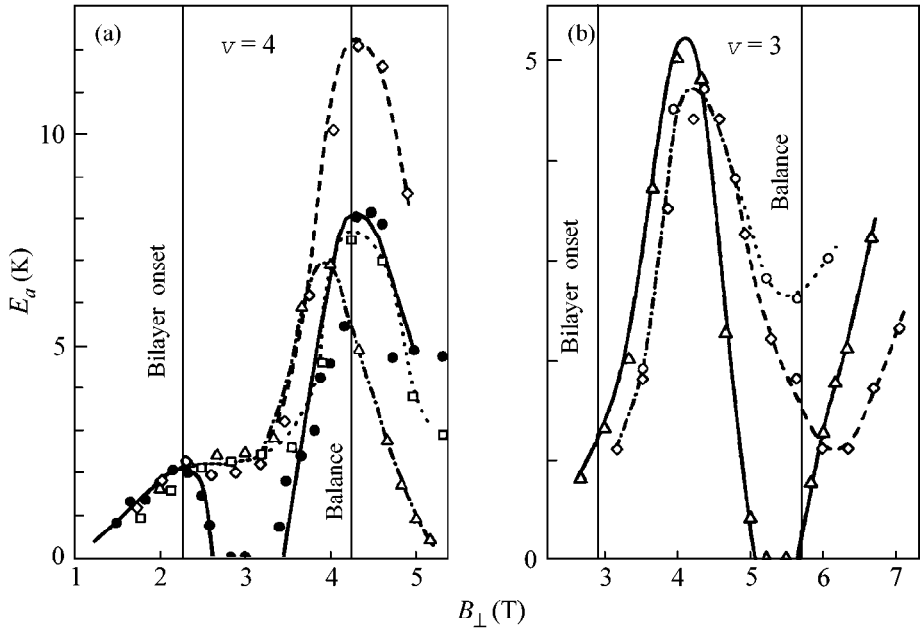

Fig. 3. Change of the activation energy with magnetic field at (a) $\nu = 4$ for $\nu = 0°$ (dots), $\Theta = 30°$ (diamonds), $\Theta = 45°$ (squares), $\Theta = 60°$ (triangles); and (b) $\nu = 3$ for $\Theta = 30°$ (circles), $\Theta = 45°$ (diamonds), $\Theta = 60°$ (triangles). The lines are guides to the eye.

tioned pinning effect at integer $\nu > 2$ cannot occur any more. Instead, as will be discussed below, the wave functions get reconstructed, which is accompanied by level splitting.

We calculate the single-particle spectrum in a tilted magnetic field in self-consistent Hartree approximation without taking into account the spin splitting (supposing small g factor), as well as the exchange and correlation energies. The intersubband charge transfer when switching on the magnetic field is a perturbation potential in the problem that mixes the wave functions for two subbands. Account is taken of a shift of the subband bottoms due to a parallel component of the magnetic field, and the value of gap at the Fermi level is determined in the first order of perturbation theory in a

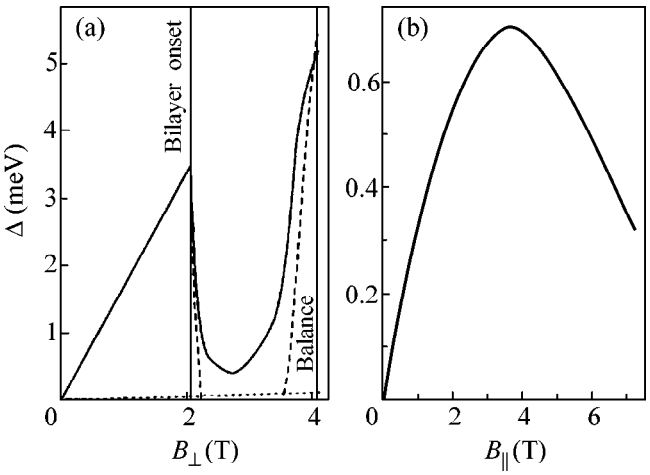

Fig. 4. The calculated gap at $\nu = 4$ as a function of magnetic field for (a) fixed tilt angle $\Theta = 0°$ (dashed line) and $\Theta = 30°$ (solid line); and (b) fixed $B_\perp = 2.6$ T. Also shown by a dotted line is the corresponding Zeeman splitting for $\Theta = 30°$.

similar way to the $\nu = 1$ and 2 cases for normal magnetic fields of [6].

The magnetic field dependence of the calculated gap Δ for filling factor $\nu = 4$ is displayed in Fig. 4. At fixed tilt angle, the calculation reproduces well the observed behavior of the gap along the $\nu = 4$ fan line (cf. Figs. 3a, 4a). The quantitative difference between the gap values can be attributed to the finite width of the Landau levels, which is disregarded in calculation.

The gap Δ as a function of parallel magnetic field component $B_\parallel$ at a fixed value of $B_\perp = 2.6$ T is depicted in Fig. 4b. It reaches a maximum at $B_\parallel = 3.5$ T and then drops with further increasing field ($B_\parallel$). It is clear that $\Delta(B_\parallel)$ reflects the dependence of the overlap of the Landau wave functions with different quantum numbers on their in-plane shift $d_0 \tan\Theta$: while at sufficiently small shifts the overlap rises with shift, at large shifts, the overlap is sure to vanish, restoring the wave function orthogonality.

The above explanation holds for filling factor $\nu = 3$ as well. We note that, in a normal magnetic field, the $\nu = 3$ gap for our case is of spin origin, since the expected spin splitting is smaller than Δ_{SAS} [6, 9]. Therefore, it can increase with $B_\parallel$ for trivial reasons. The point of importance is that the Landau wave function orthogonality has to be lost for the gap to open.

In summary, we have performed magnetocapacitance measurements on a double layer system with gate-voltage-controlled electron density distributions in tilted magnetic fields. It has been found that, for the dissipative state in normal magnetic fields at filling factor $\nu = 3$ and 4, a parallel magnetic field component leads to the opening of a gap at the Fermi level. We attribute the origin of the effect to orthogonality breaking of the Landau wave functions with different quantum numbers for two subbands as caused by a parallel magnetic field. The calculated behavior of the gap is consistent with the experimental data.

We are thankful to S.V. Iordanskiĭ for valuable discussions. This work was supported in part by the Deutsche Forschungsgemeinschaft DFG, the AFOSR (grant no F49620-94-1-0158), the Russian Foundation for Basic Research (project nos. 00-02-17294 and 98-02-16632), the program "Nanostructures" of the Russian Ministry of Sciences (project no. 97-1024), and INTAS (grant no. 97-31980). The Munich–Santa Barbara collaboration has also been supported by a joint NSF-European Grant and Max-Planck research award.

REFERENCES

1. T. Chakraborty and P. Pietilainen, Phys. Rev. Lett. **59**, 2784 (1987); D. Yoshioka, A. H. MacDonald, and S. M. Girvin, Phys. Rev. B **39**, 1932 (1989); J. P. Eisenstein, G. S. Boebinger, L. N. Pfeiffer, *et al.*, Phys. Rev. Lett. **68**, 1383 (1992); Y. W. Suen, L. W. Engel, M. B. Santos, *et al.*, Phys. Rev. Lett. **68**, 1379 (1992); Y. W. Suen, H. C. Manoharan, X. Ying, *et al.*, Phys. Rev. Lett. **72**, 3405 (1994).
2. S. Q. Murphy, J. P. Eisenstein, G. S. Boebinger, *et al.*, Phys. Rev. Lett. **72**, 728 (1994); T. S. Lay, Y. W. Suen, H. C. Manoharan, *et al.*, Phys. Rev. B **50**, 17725 (1994); S. He, X. C. Xie, S. Das Sarma, and F. C. Zhang, Phys. Rev. B **43**, 9339 (1991).
3. T. Jungwirth and A. H. MacDonald, Phys. Rev. B **53**, 9943 (1996); H. C. Manoharan, Y. W. Suen, T. C. Lay, *et al.*, Phys. Rev. Lett. **79**, 2722 (1997).
4. S. Das Sarma, S. Sachdev, and L. Zheng, Phys. Rev. B **58**, 4672 (1998); V. Pellegrini, A. Pinczuk, B. S. Dennis, *et al.*, Phys. Rev. Lett. **78**, 310 (1997); Science (Washington, D. C.) **281**, 799 (1998); V. S. Khrapai, E. V. Deviatov, A. A. Shashkin, *et al.*, Phys. Rev. Lett. **84**, 725 (2000).
5. A. G. Davies, C. H. W. Barnes, K. R. Zolleis, *et al.*, Phys. Rev. B **54**, R17331 (1996).
6. V. T. Dolgopolov, G. E. Tsydynzhapov, A. A. Shashkin, *et al.*, Pis'ma Zh. Éksp. Teor. Fiz. **67**, 570 (1998) [JETP Lett. **67**, 595 (1998)]; V. T. Dolgopolov, A. A. Shashkin, E. V. Deviatov, *et al.*, Phys. Rev. B **59**, 13235 (1999).
7. M. Hartung, A. Wixforth, K. L. Campman, and A. C. Gossard, Solid-State Electron. **40**, 113 (1996); G. Salis, B. Graf, K. Ensslin, *et al.*, Phys. Rev. Lett. **79**, 5106 (1997).
8. P. H. Beton, J. Wang, N. Mori, *et al.*, Phys. Rev. Lett. **75**, 1996 (1995).
9. V. T. Dolgopolov, A. A. Shashkin, A. V. Aristov, *et al.*, Phys. Low-Dimens. Struct. **6**, 1 (1996); V. T. Dolgopolov, A. A. Shashkin, A. V. Aristov, *et al.*, Phys. Rev. Lett. **79**, 729 (1997).

JETP Letters, Vol. 71, No. 12, 2000, pp. 500–503. Translated from Pis'ma v Zhurnal Éksperimental'noĭ i Teoreticheskoĭ Fiziki, Vol. 71, No. 12, 2000, pp. 730–735.

Oscillatory Behavior of the Resistance of Three-Layer Heteroepitaxial Mo/Nb/Mo (001) Films

G. M. Mikhaĭlov* and I. V. Malikov

Institute of Microelectronic Technology and High-Purity Materials, Russian Academy of Sciences, Chernogolovka, Moscow region, 142432 Russia

** e-mail: mikhailo@ipmt-hpm.ac.ru*

Received April 12, 2000; in final form, May 23, 2000

Electrical resistance of a three-layer heteroepitaxial Mo(35 nm)/Nb(d_{Nb})/Mo(35 nm) (001) film was found to exhibit oscillatory behavior as a function of thickness d_{Nb} of the ultrathin Nb interlayer. The oscillation period is equal to one Nb monolayer (0.16 nm). The resistance minimum of such a film corresponds to the interlayer thickness with a half-completed monolayer and is equal to the resistance of an individual Mo film of thickness 70 nm equivalent to the total thickness of the three-layer film. In this case, the three-layer film conducts as if it is a unified layer. The resistance of a three-layer film with completed Nb monolayers is maximum and equal to the resistance of two individual parallel-connected Mo films of half thickness (35 nm) each. These results are explained by the strong influence of the built-in potential, whose magnitude and scattering properties are periodic functions of the interlayer thickness. © *2000 MAIK "Nauka/Interperiodica".*

PACS numbers: 73.40.-c

INTRODUCTION

In studies of the conductivity of a metal film with thickness much smaller than the electron mean free path, electron scattering from interfaces should be taken into account. For films of thickness much greater than the Fermi wavelength $1/k_F$, one usually invokes either the classical approximation of the Fuchs model [1, 2] or the approximation of small-angle electrons (see [3] and references therein). The "specularity" $\langle p \rangle$ averaged over all conduction electrons is the key parameter of the Fuchs model:

$$\sigma_d = \sigma_o \frac{3}{4} \frac{1 + \langle p \rangle}{1 - \langle p \rangle} \frac{d}{l_o} \ln \frac{(1 - \langle p \rangle) l_0}{d}, \quad (1)$$

where σ_d, σ_o, and l_o are the film conductivity, the bulk conductivity, and the electron mean free path in bulk, respectively. The specularity parameter may be different for different electrons and may depend on the glancing angle α at the interface [3–6]:

$$p = 1 - Q(Ak_F, L_c k_F)\alpha, \quad (2)$$

where the Q parameter, determining the scattering intensity of small-angle electrons, is a function of the mean square amplitude A, the interface roughness correlation length L_c, and the Fermi wavevector k_F. According to Eq.(2), the small-angle electrons are scattered almost specularly within a certain effective angle α^* and determine the film conductivity in the small-angle electron model [3]:

$$\sigma_d = \sigma_o \frac{3\pi}{4} \alpha^*, \quad (3)$$

$$\alpha^* = \sqrt{d/Ql_o}. \quad (4)$$

In the classical approximation, the film conductivity diverges at large mean free paths l_o. In actuality, the glancing angle α, in classical terminology, may be limited by the diffraction angle α_d:

$$\alpha_d = \pi/dk_F. \quad (5)$$

If the diffraction angle (5) is comparable with the effective angle (4), the waveguide effects become substantial in the conductivity [7]. In this case, the film conductivity should be considered in terms of waveguide electron transport [8–14], even if the film thickness is much greater than $1/k_F$ and has the characteristic value [7]

$$d^* = (\pi^2 Q l_o / k_F^2)^{1/3}. \quad (6)$$

In the waveguide models [8–14], the electron wave functions have the form

$$\psi_n(z, r) = \sqrt{2/d} \sin(k_n, z) \exp(ikr), \quad (7)$$

where $k_n = (\pi/d)n$ for $n = 1, 2, 3, \ldots$; k and r are the two-dimensional in-plane electron wavevector and radius vector, respectively; and z is the coordinate along the normal to the film. The energy of the $|n, k\rangle$ state is equal to $E_{n,k} = (\hbar^2/2m)(k_n^2 + k^2)$, where m and $\hbar$ are the electron mass and Planck's constant, respectively; the $E_{n,k}$ energy is lower than the Fermi energy. In the simple limit $N_d \gg 1$, the film conductivity, with allowance

made for bulk scattering, is

$$\sigma_d = \sigma_o \frac{3\pi}{2dk_F} \sum_{n=1}^{n=N_d} \frac{1-(k_n/k_F)^2}{1+(d^*/d)^3 n^2}, \quad (8)$$

where d^* is defined by Eq. (6) and $N_d \cong dk_F/\pi$. The transition from the classical ($d > d^*$) to the quantum ($d < d^*$) limit was previously experimentally observed in the size dependence of the conductivity of W, Nb [7] and Mo, Mo–Nb [15] (001) films in the range of thicknesses $d^* \sim$ 30–50 nm much greater than $1/k_F$. The aforementioned theoretical models of waveguide transport in individual metal films were based on the isotropic approximation for free electrons. Electron umklapp processes may play an important part in electron transfer from one medium to the other or in electron reflection from the interface [16].

The influence of the structure and morphology of the outer surface of a film on the resistance was experimentally studied in [17]. We have performed analogous experiments for single-crystal metal films with a large electron mean free path in the bulk but with an interface inside them.

EXPERIMENT

Three-layer heteroepitaxial Mo(35 nm)/Nb(d_{Nb})/Mo(35 nm) (001) films were grown. The epitaxial growth of the molybdenum and niobium layers was carried out in an ultrahigh-vacuum chamber by sequential (without vacuum deterioration) laser evaporation of high-purity niobium and molybdenum targets onto a single-crystal (–1012) (*r*-plane) sapphire substrate heated to 750°C [15, 18, 19]. Schematic representation of the three-layer film structure in the form of a bridge is shown in Fig. 1 in two projections.

It is known that the Nb film (also the Mo film) deposited on the sapphire *r*-plane has the bcc structure [20], with every second monolayer being shifted along the [110] axis to the center of the projection of a bcc unit cell onto the growth plane. The spacing between the Nb layers along the [001] axis is 0.165 nm, and the lattice parameter is equal to 0.33 nm. Insofar as Mo and Nb are capable of mutual heteroepitaxy [15], the Nb interlayer was a single-crystal (001) film. Structural analysis did not detect any structural defects associated with the thin Nb interlayer or any distinctions between the upper and lower Mo layers [21].

The electron conductivity of the bridges comprised of films of length L = 1.8 mm and width W = 0.2 mm was measured by the four-probe technique over the temperature range 300–9.5 K [7]. For comparison, analogous experiments were carried out with individual single-crystal Mo (001) layers of thickness 70 nm [Mo(70 nm)] equal to the total thickness of the three-layer film and with layers of half thickness (35 nm) [Mo(35 nm)] equal to the thickness of one Mo layer in the three-layer film. The film resistivity per square $r(d)$ was determined from the formula

$$r(d) = R(d)W/L. \quad (9)$$

The resistivity measured for the longitudinal current in the three-layer Mo(35 nm)/Nb(d_{Nb})/Mo(35 nm) films exhibits oscillatory behavior as a function of the Nb interlayer thickness. The oscillation period is equal to about 0.16 nm, i.e., approximately to the spacing between the Nb monolayers. The oscillations were observed for the thicknesses d_{Nb} corresponding to 20–30 monolayers. The resistivity $r(d)$ (9) of the three-layer film is plotted in Fig. 2 as a function of thickness d_{Nb} of the Nb interlayer at temperatures 298, 150, 85, and 9.5 K. For comparison, the experimentally measured half resistivity of an individual Mo(35 nm) film (formally coinciding with the resistivity of two parallel-connected 35-nm films) and resistivity of an individual Mo(70 nm) film are also presented in Fig. 2. These values are close, respectively, to the maximum and minimum resistivity of the three-layer film. The relative oscillation amplitude at 298 K is equal to 15% and increases to 50% and more and eventually becomes saturated on lowering the temperature to 9.5 K. The resistivity minima of the three-layer film are observed for interlayer thicknesses corresponding to every subsequent half-completed Nb monolayer. The resistivity of the three-layer film with completed Nb monolayers is maximum, excluding the initial portion in the vicinity of zero d_{Nb}.

RESULTS AND DISCUSSION

It follows from the observed oscillatory behavior of the electrical conductance of the three-layer Mo(35 nm)/Nb(d_{Nb})/Mo(35 nm) (001) film with vari-

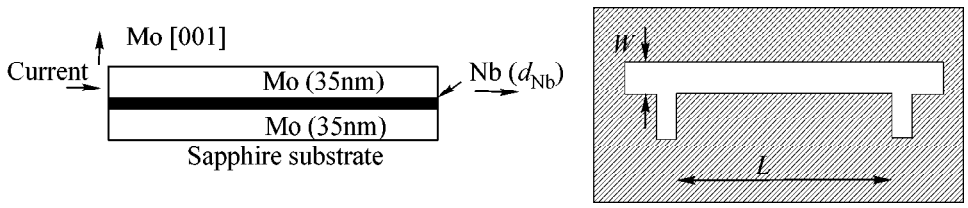

Fig. 1. Schematic representation of the three-layer bridge in two projections.

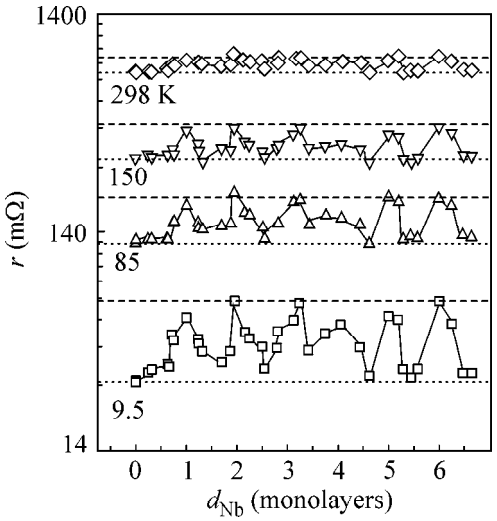

Fig. 2. Resistivity of the three-layer heteroepitaxial Mo(35 nm)/Nb(d_{Nb})/Mo(35 nm) (001) film as a function of thickness d_{Nb} of the Nb interlayer at temperatures 298, 150, 85, and 9.5 K. The dashed lines indicate half resistivities of an individual 35-nm-thick Mo film, and the dotted lines indicate the resistivities of an individual Mo film of thickness 70 nm at the respective temperatures.

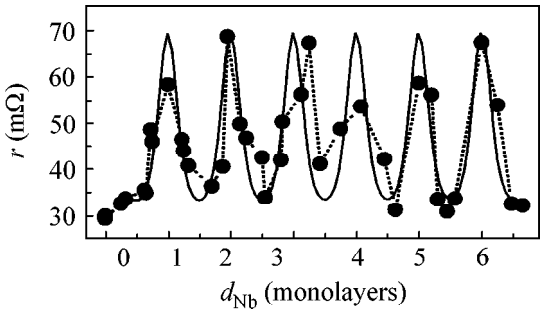

Fig. 3. Resistivity of the three-layer film vs. thickness (d_{Nb}) of the Nb interlayer: (dots and dashed lines) experimentally measured at 9.5 K and (solid line) plotted according to Eq. (10).

able thickness of the ultrathin Nb interlayer that the system conducts either as an individual Mo(70 nm) film of the same total thickness or as two separate parallel-connected Mo(35 nm) films of half thicknesses. Accordingly, the inner-film potential depends on the thickness of the Nb interlayer in a periodic manner and either goes "unheeded" for the conduction electrons or behaves as a scatterer, like the outer boundary of the Mo(35 nm) film.

The maxima in the resistance oscillations observed in [17] for epitaxial films corresponded to the half-monolayer metal coating. It was assumed that the outer surface of the initial film was nearly specular, while the additional coating gave rise to a rough (at the atomic level) surface. As a result, the average specularity parameter $\langle p \rangle$ in Eq. (1) changed periodically, leading to the oscillations in the film resistance. In our case, the resistance oscillations can be explained in the same way if we assume that the Nb interlayer is impenetrable to electrons but its roughness (specularity) is a periodic function of thickness. In the waveguide model, the transverse electron motion in the three-layer film is regarded as a motion in two coupled quantum wells, so that the electronic states can be classified according to the odd and even wave functions, the latter having an antinode at the interlayer. Taking this into account, the observed resistance oscillations in the three-layer film could also be explained by the strong scattering of the even states and hence their periodic "dropout" from conduction. However, such an explanation faces problems, because the resistance maxima of the three-layer film correspond to the completed Nb monolayers, and hence the specularity maxima (roughness minima) correspond to the resistance maxima.

We assume that the oscillatory dependence is caused by the fact that, in addition to the scattering properties of the built-in potential, the probability of electron transmission from one Mo layer to the other also changes. The small-angle electrons can be localized in either of the Mo layers and transmit, either partially or completely, through the Nb layer without being scattered by the low barrier of the contact potential. Evidently, the resistivities of the three-layer film and an individual Mo film with identical total thickness should be the same in the latter case, as was actually observed in the experiment. If the probability of small-angle electron transmission through the Nb interlayer is close to zero, then the Mo layers in the three-layer film conduct independently, while the intensity of electron-momentum dissipation along the current is the same for all interfaces. This is possible if the potential fluctuations are caused by film bending dictated by the substrate relief. As a result, the d^* parameter in Eq. (8) is identical for all Mo layers, so that Eq. (8) can be used for each of the half-thick (35 nm) Mo layers, and the whole structure can be regarded as two parallel-connected Mo(35 nm) films. In the intermediate case of a partially penetrable barrier, the waveguide model (8) should be developed for such a three-layer film. We propose the following dependence on the interlayer thickness d_{Nb} for the resistivity of a three-layer film of total thickness d_{Nb}:

$$r(d, d_{Nb}) = 0.5r(d/2)D(d_{Nb}) + r(d)(1 - D(d_{Nb})), \quad (10)$$

where $r(d/2)$ and $r(d)$ are the resistivities of individual Mo films of half and total thickness, respectively, and $D(d_{Nb}) = \exp(-4d_o k_o \sin^2(\pi d_{Nb}))$ is the probability of electron transmission from one Mo layer to the other. The $4d_o k_o$ value is determined by the potential barrier width and height at the Mo–Nb and Nb–Mo interfaces. For a barrier width equal to the spacing $d_o \sim 0.16$ nm between the monolayers and a barrier height equal to

the work function $\Delta V = 0.5$ eV [22] between Mo and Nb (001), one has $k_o = (2m(\Delta V - E_{n,o})/\hbar^2)^{1/2} \approx 3.6$ nm^{-1} and $4d_o k_o \cong 2.4$, where $E_{n,o} = E_{n,k}(k = 0) \sim 0.01$ eV is the energy of transverse electron motion at $n \sim 1$. The dependence (10) in the range of thicknesses from 0.5 to 6.5 monolayers is shown in Fig. 3 for $4d_o k_o = 2.4$ and the values of $r(d = 35\ \text{nm}) = 0.138\ \Omega$ and $r(d = 70\ \text{nm}) = 0.0296\ \Omega$ determined experimentally at 9.5 K. The experimentally measured resistivities of the three-layer film at 9.5 K are also shown in Fig. 3. Equation (10) agrees satisfactorily with the experiment, except for the initial portion of the curve where the d_{Nb} values are smaller than one-half monolayer, which can be regarded as a transition layer in the formation of the built-in potential.

CONCLUSIONS

The experimental results on the oscillatory behavior of the resistance of a three-layer heteroepitaxial Mo/Nb/Mo (001) film with variable thickness of the Nb interlayer and the proposed explanation indicate that the scattering of small-angle electrons from the spatial fluctuations of the potential built into the three-layer film by the Nb interlayer plays an important role. The Nb interlayer forms a scattering potential that changes, with a period of one monolayer, from the minimum to the maximum value with changing thickness d_{Nb}. As a result, the wave functions of small-angle electrons periodically change, so that the intensity of conduction electron scattering from the fluctuations of the built-in potential changes, giving rise to the oscillations in the film resistance. The resistance maxima of the three-layer film correspond to the Nb interlayer with completed monolayers; in this case, the film conducts as two separated parallel-connected Mo films of half thickness each. The resistance minima of the three-layer film correspond to a half-completed monolayer in the Nb interlayer; in this case, the film conducts as if it were a unified layer, while its resistance and the resistance of an individual Mo layer of the same total thickness are equal to each other.

This work was supported by the program "Physics of Solid-State Nanostructures," (project no. 99-1126), the Russian Foundation for Basic Research (project no. 00-02-16601), and the INTAS (grant no. 99-193).

REFERENCES

1. K. Fuchs, Proc. Cambridge Philos. Soc. **34**, 100 (1938).
2. H. Sondheimer, Adv. Phys. **1**, 1 (1952).
3. L. A. Falkovsky, Adv. Phys. **32**, 753 (1983).
4. R. F. Green, in *Solid State Surface Science*, Ed. by M. Green (Marcel Dekker, New York, 1970; Mir, Moscow, 1972).
5. A. F. Andreev, Usp. Fiz. Nauk **105**, 113 (1971) [Sov. Phys. Usp. **14**, 609 (1972)].
6. Yu. P. Gaĭdukov, Electronic Properties of Whiskers, in *Conduction Electrons*, Ed. by M. I. Kaganov and V. S. Édel'man (Nauka, Moscow, 1985), Chap. 12.
7. G. M. Mikhaĭlov, I. V. Malikov, and A. V. Chernykh, Pis'ma Zh. Éksp. Teor. Fiz. **66**, 693 (1997) [JETP Lett. **66**, 725 (1997)].
8. Z. Tesanovic, M. V. Jaric, and S. Maekawa, Phys. Rev. Lett. **5**, 2760 (1986).
9. N. Trivedi and N. W. Ashcroft, Phys. Rev. B **38**, 12298 (1988).
10. G. Fishman and D. Calecki, Phys. Rev. Lett. **62**, 1302 (1989).
11. G. Fishman and D. Calecki, Phys. Rev. B **43**, 11581 (1991).
12. N. M. Makarov, A. V. Moroz, and V. A. Yampol'skiĭ, Phys. Rev. B **52**, 6087 (1995).
13. X.-G. Zhang and W. H. Butler, Phys. Rev. B **51**, 10085 (1995).
14. A. E. Meyerovich and A. Stepaniants, Phys. Rev. B **60**, 9129 (1999).
15. I. V. Malikov and G. M. Mikhaĭlov, Thin Solid Films **355–356**, 1 (1999).
16. V. F. Gantmakher and I. B. Levinson, in *Scattering of Charge Carriers in Metals and Semiconductors* (Nauka, Moscow, 1984), Chap. 11.
17. D. Schumacher, *Surface Scattering Experiments with Conduction Electrons* (Springer-Verlag, Berlin, 1993).
18. G. M. Mikhaĭlov, I. V. Malikov, and V. T. Petrashov, Fiz. Tverd. Tela (St. Petersburg) **38**, 3212 (1996) [Phys. Solid State **38**, 1754 (1996)].
19. I. V. Malikov and G. M. Mikhaĭlov, J. Appl. Phys. **82**, 5555 (1997).
20. G. Oya, M. Koishi, and Y. Sawada, J. Appl. Phys. **60**, 1440 (1986).
21. G. M. Mikhaĭlov, I. V. Malikov, A. V. Chernykh, *et al.*, in *Proceedings of the 7th International Symposium on Nanostructures: Physics and Technology, St. Petersburg, 1999*, p. 99.
22. *Physical Quantities: Handbook*, Ed. by I. S. Grigor'ev and E. Z. Melikhov (Énergoizdat, Moscow, 1991).

Translated by V. Sakun

JETP Letters, Vol. 71, No. 12, 2000, pp. 504–507. Translated from Pis'ma v Zhurnal Éksperimental'noĭ i Teoreticheskoĭ Fiziki, Vol. 71, No. 12, 2000, pp. 736–740.

Critical Current in Superconducting Quantum Point Contacts

N. M. Shchelkachev

Landau Institute for Theoretical Physics, Russian Academy of Sciences, ul. Kosygina 2, Moscow, 117940 Russia
e-mail: nms@landau.ac.ru

Received May 23, 2000

The quantization of the critical current I_c in a quantum point contact is studied on varying the number of free channels (varying the constriction width d_0 in 2DEG). It is shown that the shape of the quantum I_c is not universal and depends on the parameters of the contact, in particular, on the properties of the 2DEG–S boundaries. Because of the effect of normal reflection from the S–2DEG boundaries, the quantum critical current nonmonotonically depends on d_0 and may have a resonance structure. If E_F coincides with a quasi-stationary level of the square potential well formed by the contact walls, the critical current has a local maximum (resonance) equal (in the first channel) to the ratio of the electron charge to its time of travel through the contact. The critical current at the maximum is determined by the lowest positive Andreev level (for the phase difference π). © *2000 MAIK "Nauka/Interperiodica".*

PACS numbers: 74.80.Fp; 72.10.-d; 74.50.+r

Quantization of the critical current I_c was observed in recent experiments on ballistic Josephson junctions of the superconductor (S)–two-dimensional electron gas (2DEG)–superconductor (S) type with a microconstriction in the normal part when the constriction width d_0 in 2DEG was varied by changing the gate voltage [1]. With increasing d_0, the number of open transversal channels in the constriction increased; therefore, the $I_c(d_0)$ dependence exhibited a steplike behavior. The shape and the height of the I_c step (quantum) depended on the contact parameters. It is interesting that at certain d_0 the critical current had a resonance structure with local maxima and minima. Calculations [2] showed that the quantum I_c does not depend on the parameters characterizing the contact geometry and equals $e\Delta/\hbar$ only in a narrow ($\xi_0 \gg L$) and perfect contact. Here, $\xi_0 = \hbar v_F/\pi\Delta$, L is the distance between the superconductors, and Δ is the gap at absolute zero. The term "perfect" contact means that there is no normal scattering of quasiparticles (electrons and holes) from the NS boundary at excitation energies $|E| < \Delta$. It is shown numerically in [3] that the quantization of I_c is not universal even in an ideal contact under the condition that $\xi_0 \gtrsim L$, and the resonances in I_c mentioned above arise from contact imperfection, namely, the effects of normal scattering of quasiparticles from the gate potential, Schottky-type barriers at the 2DEG–S boundary, etc. The current quantization in a perfect S–2DEG–S contact was studied (analytically) in [4] and that in an imperfect but narrow ($L \ll \xi_0$) contact, in [5]. However, the experiment [1], in which the quantization of the critical current was observed, was carried out with an imperfect contact in which $L \lesssim \xi_0$, and resonances (Fabry–Perot oscillations in terms of [1]) were seen in the $I_c(d_0)$ dependence.

It remains unclear how to describe the quantization of the critical current in imperfect contacts; that is, what is the functional dependence $I_c(d_0)$ for a sufficiently extensive selection of contact parameters; at which d_0 values does the critical current have a resonance (local maximum); what is the amplitude of the critical current at the resonance; for which parameters of the contact are the I_c resonances weak; etc.? This work is devoted to developing approaches to the solution of the above problems.

Because of Schottky barriers, differences in the electron Fermi momenta in S and 2DEG, etc., the potential barriers arise at the 2DEG–S boundary, leading to normal scattering of quasiparticles (electrons and holes) from the boundaries (even if the energy of the quasiparticles is lower than Δ). This effect is the reason for the nonmonotonic dependence of I_c on the constriction width d_0 [3]. It turns out that I_c is a maximum at d_0 values corresponding to the resonance of the probability of electron tunneling through a potential box restricted by the given barriers that coincides with E_F. This conclusion is true for any barrier penetrability. At the maximum, the critical current is equal to the ratio of the electron charge to its time of travel (with an energy equal to E_F) from one superconductor to another. It is worth noting that only quasiparticles at the lowest (positive) Andreev level [6] make a contribution to the critical current when the phase difference between the semiconductors $\varphi = \pi - 0$.

The Josephson current in a superconducting quantum point contact (SQPC) can be described in terms of

quasiparticles (electrons and holes) whose wave functions $u(x, y)$ and $v(x, y)$ obey the Bogolyubov–de Gennes (B–dG) equation [7]. Let us choose the x axis in the 2DEG plane along the current direction perpendicular to the 2DEG–S boundary and the y axis parallel to this boundary (see Fig. 1). We will describe the pairing potential with the use of the $\Delta(x, y) = \Delta\exp\{i\varphi\Theta(x - L/2)\}\Theta(|x| - L/2)$ anzatz [3] [$\Theta(x) = 1$, if $x > 0$; $\Theta(x) = 0$ otherwise]. Let us assume that the constriction width $d(x)$ smoothly varies and the variables in the B–dG equations can be adiabatically separated in the same way as it was done in [4]. Thus, in the constriction, $u(x, y) = \sqrt{2/d(x)}\sin(\pi j(y/d(x) + 1/2))u(x)$, $j = 1, 2$ [similarly for $v(x, y)$]. Now, $u(x)$ and $v(x)$ obey a one-dimensional B–dG equation. The potentials (walls) $V(x + L/2)$ and $V(-x + L/2)$ localized at the 2DEG–S boundary will account for the effect of normal reflection [8]. The potential $V(x)$ is characterized by the energy-independent scattering matrix with tunneling amplitudes $t = t'$ and reflection amplitudes r and r' (the primed amplitudes describe the scattering of electrons incident from the right). The transversal quantization energy $E_\perp(x) = (\hbar\pi j)^2/2m_N d^2(x)$ accounts for the gate effect on electrons in 2DEG. Hence, the wave vector of quasiparticles in the constriction equals $k_{N,\pm}(x) = \sqrt{2m_N(\mu_N \pm E - E_\perp(x))/\hbar^2}$ (m_N is the effective electron mass in 2DEG). The open channels with the subscript j such that $\mathrm{Im}\,k_{N,\pm} = 0$ make the major contribution to the current [4]. It is convenient to introduce a potential U composed of the V and $E_\perp(x)$ walls. It is characterized by a scattering matrix similar to that for a Fabry–Perot interferometer. For example, the amplitude of electron (hole) tunneling through this potential $t_U = t^2\exp\{i(\sqrt{2m_S(\mu_S \pm E)} - \sqrt{2m_N(\mu_N \pm E)})L/\hbar\}/(1 - (r')^2\exp(2iS_\pm))$, where $S_\pm = \int_{-L/2}^{L/2} k_{N,\pm}(x)dx$ is the action. The quantity $D_U = |t_U|^2$ has the meaning of the probability of electron tunneling through 2DEG. Within the adiabatic approximation, the channel mixing in the contact can be neglected; therefore, the contribution to the Josephson current from each channel can be searched independently [9].

The Josephson current $I(\varphi)$ in the channel j can be expressed through the amplitude of Andreev reflection of an "electron" quasiparticle from SQPC according to [3]. This gives the following result for the Josephson current:

$$I(\varphi) = T\sum_{\omega} J(\omega, \varphi) = T\sum_{\omega_k}\frac{2e}{\hbar}\frac{\partial}{\partial\varphi}\ln(g(i\omega_k, \varphi)), \quad \omega_k = T\pi(2k + 1), \quad k = 0, \pm1, \ldots, \tag{1}$$

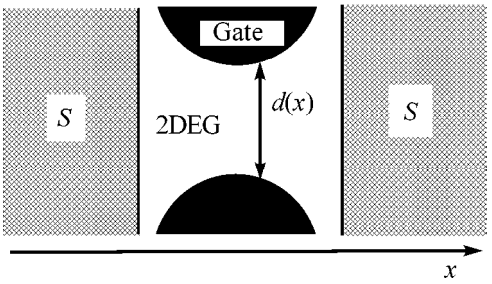

Fig. 1. Schematic picture of a Josephson point contact.

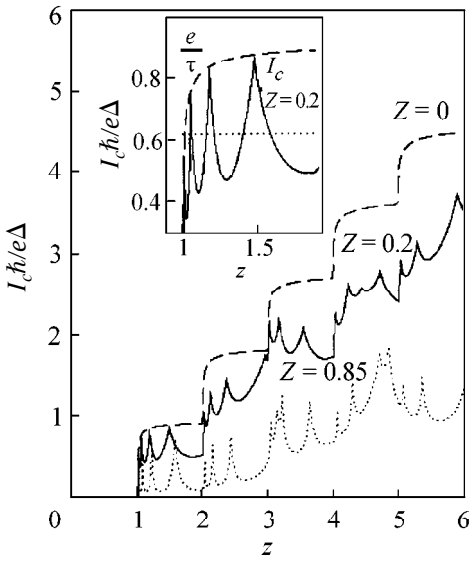

Fig. 2. Critical current I_c at different values of parameter Z characterizing the barrier penetrability at the 2DEG–S boundary. The inset shows I_c at $Z = 0.2$ and the function (4) coinciding with $z = 2d_0/\lambda_f$.

$$g(E, \varphi) = D^2\cos(\varphi) + 2R\cos(\beta) - \cos(2\gamma - \beta) - R^2\cos(2\gamma + \beta) - 4R\sin^2(\gamma)\cos(\beta_0), \tag{2}$$

$$\gamma = \arccos(E/\Delta), \quad \beta = S_+ - S_-, \quad \beta_0 = 2\arg(r) + S_+ + S_-, \tag{3}$$

where $D = |t|^2 = 1/(1 + Z^2)$, and $R = |r|^2$ is the probability of quasiparticle tunneling and reflection from the potential V.

Equations (1)–(3) are the central result of this work, because they give an insight into how the critical current depends on the contact parameters. Let us assume that one channel with $j = 1$ is open; that is, we will study the first step (see Fig. 2) of the critical current. At zero temperature, if the resonance level of the potential box formed by the 2DEG–S boundaries (potential walls V) coincides with E_F [mathematically, this is written as

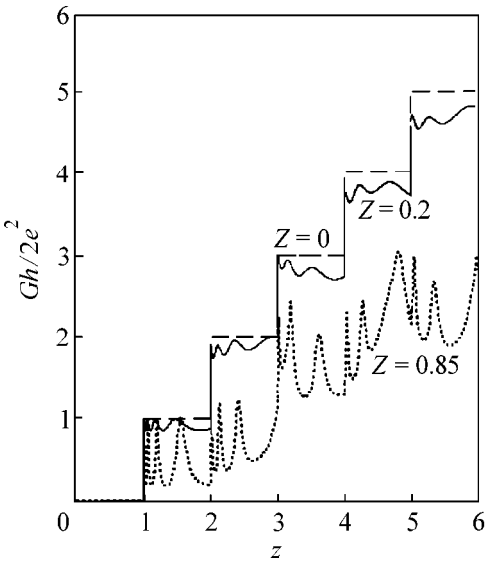

Fig. 3. Conductance G of the contact at various Z in the limit $\Delta = 0$.

follows: $\beta_0|_{E=0} = 2\pi n$, $n = 0, 1, \ldots \Leftrightarrow D_U(E = 0) = 1$], it follows from Eq. (1) that

$$I_c = |I(\pi - 0)| = \frac{e}{\tau}, \quad \tau = \frac{\hbar}{\Delta} + \tau_0 \frac{R+1}{D}, \qquad \tau_0 = (\hbar \partial_E S_+|_{E\to 0}). \tag{4}$$

This equation gives the critical current magnitude at the point of its local maximum (resonance) as a function of the constriction width d_0.

Equation (4) can be pictorially interpreted as follows. An electron wave packet (at E_F) undergoes Andreev reflection from the 2DEG–S boundary and transforms into a hole wave packet in the time $\hbar/(2\Delta)$. The τ value is the time it takes for an electron at E_F to travel from one superconductor to another (within the quasiclassical approximation), τ_0 is the half-period of the classical motion of an electron in the potential box formed by the walls V, and $(R + 1)/D$ can be interpreted as the number of attempts made by the electron to escape from this potential box. Then, τ has the meaning of the time it takes for a Cooper pair decayed in one of the superconductors and transformed into two electrons in 2DEG (into the electron and hole quasiparticles) to transform into a Cooper pair in another superconductor.

If E_F does not exactly coincide with the resonance level, the equation for I_c (4) must be multiplied by $1 - |\sin(\beta_0/2)|2\sqrt{R}/D$, where $|\sin(\beta_0/2)|2\sqrt{R}/D \ll 1$. At $D \ll 1$, the applicability limit of Eq. (4) (the width of the critical current resonance as a function of d_0) is $\delta d_0 \propto D/\partial_{d_0} S_+ \sim d_0 D/(\tau_0 \hbar/2m d_0^2)$. At $R \ll 1$, Eq. (4) describes the critical current at any d_0 [4]. In this case, the results for I_c obtained previously in [2] at $\tau_0 \ll \tau_\Delta$ and in [10] at $\tau_0 \gg \tau_\Delta$ follow from Eq. (4). If $D \ll 1$, Eq. (4) gives the equation for I_c obtained in [11].

The equation $g(E, \varphi) = 0$ (2) has Andreev levels as a solution. From this equation, it follows that only the lowest Andreev level, which coincides with E_F at $\varphi = \pi$, contributes to I_c [Eq. (4)]. That is, there exists such an Andreev level that $|2(\partial_\varphi E_0(\varphi)/\hbar)_{\varphi\to\pi-0}| = e/\tau$ [see Eq. (4)]. (In the limit $D \ll 1$, this result was also obtained in [5] at $L \ll \xi_0$ and in [11].)

If the contact parameters deviate from the condition $\beta_0(E = 0) = 2\pi n$ (I_c resonance), the critical current decreases. At the I_c minimum, that is, when $\beta_0|_{E\to 0} = 2\pi(n + 1/2)$ and under the conditions $D \ll 1$ and $\tau_0 \gg \tau_\Delta$, $I_c = (e/\tau)D/4\pi$. If the last condition is replaced by $\tau_0 \ll \tau_\Delta$, then $I_c = (e/\tau_\Delta)D^2/8$. In both cases, the Josephson current depends on the phase as $I(\varphi) \propto \sin(\varphi)$.

Equation (4) is valid at $T \ll \hbar/\tau$. If $\hbar/\tau \ll T \ll \hbar/\tau_0$, the resonance of the probability of electron tunneling through the normal part of the contact (through the potential U) occurs at E_F, and this resonance is sharp [the resonance width $\Gamma = \hbar/\tau$ is well below the distance $\pi\hbar/\tau_0$ between the resonances, see Eq. (4)], then the Josephson current $I(\varphi) = (e\Gamma\sin(\varphi/2)/\hbar)\tanh(\Gamma\cos(\varphi/2)/2T)$ and $I_c \approx (e\Gamma/\hbar)(\Gamma/4T)$ at $T \gg \Gamma$. If $\hbar/\tau_0 \ll T \ll \Delta$ then the Josephson current decays exponentially with temperature as $\propto \exp(-2\pi T\tau_0/\hbar)$. Here, $2\pi T\tau_0/\hbar \gg 1$.

It was assumed above that only the first channel is open. If many channels are open, then, in order to obtain the critical current at $D = 1$, the expression for I_c in Eq. (4) must be summed over all open channels j. The dependence of the critical current on d_0 will mainly be determined by the open channel with the largest subscript j [4]. At $D \ll 1$, the maximum critical current can be obtained by summing e/τ over the channels obeying the maximum condition [see Eq. (4)]. At the minimum, I_c is equal to the sum over the open nonresonance channels ($\beta_0 \neq 2\pi n$) from $(e/\tau)D/4\pi$ if $\tau_0 \ll \hbar/\Delta = \tau_\Delta$ and from $(e/\tau_\Delta)D^2/8$ under the condition that $\tau_0 \gg \tau_\Delta$. For the case $D \lesssim 1$, the curves for the critical current are constructed in Fig. 2. It was assumed that $S_+ = \sqrt{2m_N L^2(\mu(1 - j^2/z^2) + E)}/\hbar$, $T = 0$, $\Delta = 15.3 \times 10^{-4}$ eV, $L = 0.04$ μm, $\mu = \pi\hbar^2 N/m_N$, $N = 2.3 \times 10^{12}$ cm^{-2} in 2DEG, and $m_N = 0.045 m_e$. The conductance G of the given contact at $\Delta = 0$ is plotted in Fig. 3. The figure shows that the G quanta depend on the contact parameters (on Z). The reason for this behavior is the scattering of electrons from the S–2DEG barriers located at distances from the constriction smaller than the length L_ϕ of electron dephasing. In [12], where the conductance quantization was studied, the scattering was small; therefore, the G quanta assumed a universal value of $2e^2/h$.

The author is grateful to G.B. Lesovik for useful and stimulating discussions and to G. Blatter, D. Kuhn, and M.V. Feĭgel'man. It is to Lesovik's interest that this

article owes its appearance. This work was supported by the Russian Foundation for Basic Research, project no. 00-02-16617.

REFERENCES

1. H. Takayanagi, T. Akazaki, and J. Nitta, Phys. Rev. Lett. **75**, 3533 (1995).
2. C. W. J. Beenakker, Phys. Rev. Lett. **67**, 3836 (1991).
3. A. Furusaki, H. Takayanagi, and M. Tzukada, Phys. Rev. Lett. **67**, 132 (1991); Phys. Rev. B **45**, 10563 (1992).
4. N. M. Chtchelkatchev, G. B. Lesovik, and G. Blatter, cond-mat/9907460; Phys. Rev. B (in press).
5. P. Samuelsson, J. Lantz, V. S. Shumeĭko, *et al.*, cond-mat/9904276.
6. A. F. Andreev, Zh. Éksp. Teor. Fiz. **46**, 1823 (1964) [Sov. Phys. JETP **19**, 1228 (1964)].
7. P. G. De Gennes, *Superconductivity of Metals and Alloys* (Benjamin, New York, 1966; Mir, Moscow, 1968).
8. U. Schlüssler and R. Kümmel, Phys. Rev. B **47**, 2754 (1993).
9. L. I. Glazman and A. V. Khaetskii, J. Phys.: Condens. Matter **1**, 5005 (1989).
10. I. O. Kulik, Zh. Éksp. Teor. Fiz. **57**, 1745 (1969) [Sov. Phys. JETP **30**, 944 (1970)]; C. Ishii, Prog. Theor. Phys. **44**, 1525 (1970).
11. D. Kuhn, N. M. Chtchelkatchev, G. B. Lesovik, *et al.* (unpublished).
12. B. J. van Wees, H. van Houten, C. W. J. Beenakker, *et al.*, Phys. Rev. Lett. **60**, 848 (1988); D. A. Wharam, T. J. Thornton, R. Newbury, *et al.*, J. Phys. C **21**, L209 (1988); L. I. Glazman, G. B. Lesovik, D. E. Khmel'nitskiĭ, *et al.*, Pis'ma Zh. Éksp. Teor. Fiz. **48**, 218 (1988) [JETP Lett. **48**, 238 (1988)].

Translated by A. Bagatur'yants

JETP Letters, Vol. 71, No. 12, 2000, pp. 508–510. Translated from Pis'ma v Zhurnal Éksperimental'noĭ i Teoreticheskoĭ Fiziki, Vol. 71, No. 12, 2000, pp. 741–744.

Totally Symmetric Vibrational Modes of Fullerene C_{60}

O. N. Bubel', S. A. Vyrko, E. F. Kislyakov, and N. A. Poklonskiĭ*

Belarussian State University, Leningradskaya ul. 14, Minsk, 220072 Belarus

** e-mail: poklonski@phys.bsu.unibel.by*

Received May 24, 2000

Semiempirical molecular orbital calculations are carried out for the totally symmetric vibrations of the C_{60} molecule. The calculated equilibrium geometry coincides with the precision experimental data to within measurement error. The ratio of force constants calculated for the two different types of C–C bonds in fullerene is equal to 1.389. A comparison of the computational results with the Raman scattering data indicates that there may be Fermi resonance between the totally symmetric vibrations. © *2000 MAIK "Nauka/Interperiodica".*

PACS numbers: 36.40.Qv; 33.20.Fb; 61.46.+w

Because of high symmetry, the C_{60} molecule is subject to various instabilities associated with both interaction between electronic and nuclear degrees of freedom (Jahn–Teller effect [1]) and interaction of various vibrational modes with one another (Fermi resonance [2, 3]). These instabilities determine the properties of fullerene-based materials, in particular, the superconducting transition temperature of fullerites M_3C_{60}, where M stands for an alkali-metal atom [4].

The results of Raman scattering measurements carried out for fullerenes C_{60} with an accuracy sufficient for quantitative analysis of the fine structure of the spectral lines are presented in [5]. The origin of the fine structure of the line corresponding to the high-frequency totally symmetric $A_g(2)$mode remains to be clarified. The totally symmetric A_g mode is also of interest, because it is Jahn–Teller active in the C_{60}^{n-} ions.

The purpose of this work is to elucidate the qualitative features of the totally symmetric vibrational modes of the C_{60} molecule. The molecular orbital method (the MOPAC 7.0 program [6] with PM3 parameterization) was used.

Normal coordinates of the totally symmetric vibrations. Figure 1 displays the C_{60} molecule as a frustum of an icosahedron. The dashed lines show the truncated parts of the icosahedron, and the circles denote the C atoms.

The bonds in the C_{60} molecule are of two types [7]. The l_p bonds coincide with the pentagon sides lying in the planes of truncation; l_h are the bonds between the pentagon vertices and coincide with the frustum edges. It is usually assumed that the l_h bond is close in character to the double C–C bond and l_p is close to the ordinary bond.

Let us draw a section passing through the polar vertices and an edge of the icosahedron. There are a total of 15 of such sections in the icosahedron. One-half of one of these sections is shown in Fig. 2.

To describe the fullerene vibrations, we choose a Cartesian coordinate system with the origin in the center of the molecule in the sectional plane. The *OX* axis is directed parallel to the l_h bond. The totally symmetric molecular vibrations are described by two independent parameters, for which we take the Cartesian coordinates *x* and *z* of a carbon atom. The kinetic energy of 60 carbon atoms is

$$K = 60\frac{m}{2}[(\Delta\dot{x})^2 + (\Delta\dot{z})^2], \quad (1)$$

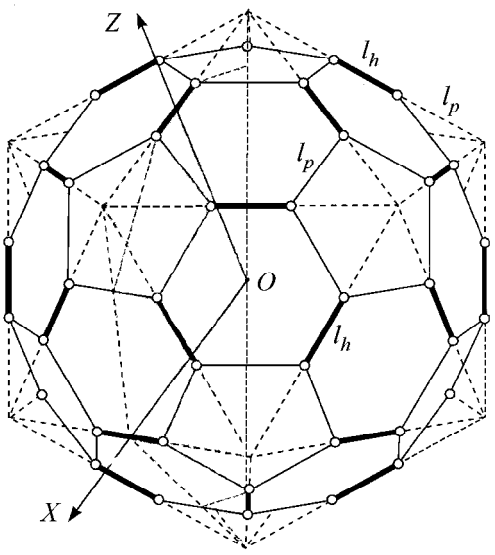

Fig. 1. The C_{60} fullerene molecule. The light circles are the carbon atoms, the solid lines are the C–C bonds, thin lines are for l_p, and heavy lines are for l_h. The dashed lines indicate the truncated parts of the icosahedron. One of the 30 half-planes, in which the carbon atoms move without violating icosahedron symmetry, is shaded.

0021-3640/00/7112-0508$20.00

where Δx and Δz are the projections of the displacement of a carbon atom of mass m from the equilibrium position.

In the harmonic approximation, the sum of the potential energies of the C–C bonds is

$$U = 30\frac{k_h}{2}(\Delta l_h)^2 + 60\frac{k_p}{2}(\Delta l_p)^2, \quad (2)$$

where k_h and k_p are the bond force constants and Δl_h and Δl_p are the deviations of bond lengths from their equilibrium values.

One can see from Figs. 1 and 2 that the icosahedral symmetry is conserved for the moving carbon atoms if

$$\Delta l_h = 2\Delta x, \quad \Delta l_p = \Delta z\cot\alpha - \Delta x, \quad (3)$$

where $1/\cos\alpha = 2\cos 18°$ (see, e.g., [7]). Combining Eqs. (1) and (2) and taking into account Eq. (3), one obtains the following Hamiltonian for the totally symmetric vibrations of fullerene:

$$H = 60\frac{m}{2}[(\Delta\dot{x})^2 + (\Delta\dot{z})^2] \times 30\frac{k_h}{2}(2\Delta x)^2 + 60\frac{k_p}{2}(\Delta z\cot\alpha - \Delta x)^2. \quad (4)$$

The rotation of the Δx and Δz coordinates through an angle

$$\varphi = \frac{1}{2}\arctan\left(\frac{2}{\cot\alpha - (2\gamma+1)\tan\alpha}\right), \quad (5)$$

where $\gamma = k_h/k_p$, transforms Eq. (4) to the diagonal form. Equation (5) determines the dependence of the fullerene normal coordinates $\Delta x'$ and $\Delta z'$ on the force constant ratio γ.

Molecular orbital calculation of fullerene. The PM3 calculation of the equilibrium geometry of C_{60} yields the values $l_h = 1.384$ Å and $l_p = 1.458$ Å coinciding with the experimental data [8] with an accuracy of measurements at liquid helium temperature. As to the calculations of the fundamental vibrations of fullerene in the harmonic approximation, the corresponding results, as well as those of the MNDO calculations [10], are at variance with the experimental data [9]. The discrepancy is particularly large between the calculated frequencies of the totally symmetric vibrations $A_g(1) = 623$ cm^{-1} and $A_g(2) = 1752$ cm^{-1} and the measured [5] $A_g(1) = 497$ cm^{-1} and $A_g(2) = 1468$ cm^{-1} values. To reveal the origin of this discrepancy, we calculated the potential energy surface for the totally symmetric modes up to the ±0.04 Å deviations of the C–C bond lengths from their equilibrium values. The use of Eq. (5) in the investigation of the potential energy surface yields $k_h/k_p \approx 1.389$. The normal coordinates corresponding to this γ value are depicted in Fig. 2. One can see that one of the normal vibrations is a breathing mode, while the other corresponds approximately to the carbon atoms sliding along the edges of a frustum of the icosahedron.

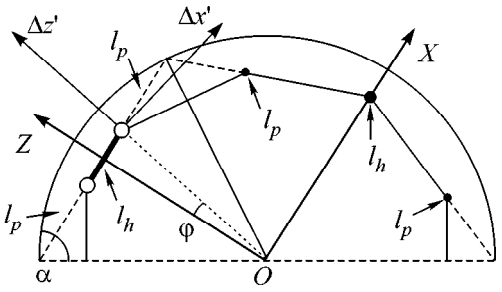

Fig. 2. Section of the fullerene molecule. The black circles are the intersections with the C–C bonds; the thin solid lines are the intersections with the faces of the frustum of the icosahedron; $\Delta x'$ and $\Delta z'$ are the normal coordinates of the totally symmetric vibrations (for the remaining notations, see Fig. 1 and the text).

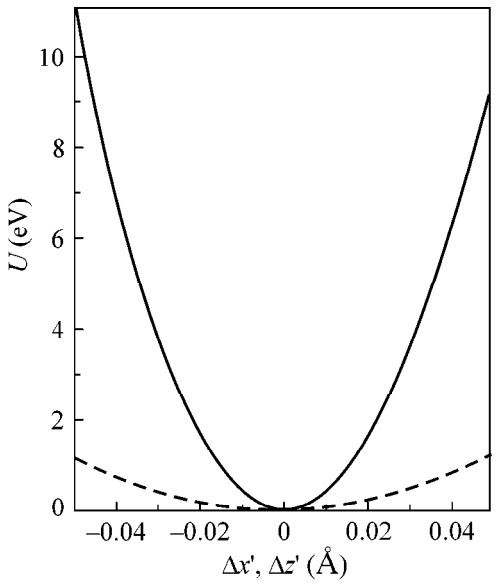

Fig. 3. Fullerene energy U as a function of the normal coordinates $\Delta x'$ and $\Delta z'$. The solid line corresponds to the high-energy mode $A_g(2)$, and the dashed line corresponds to the breathing mode $A_g(1)$. The energy of the equilibrium geometrical configuration is taken as the U origin.

The results of the potential energy surface calculations are presented in Fig. 3 as functions of normal coordinates. The curves are noticeably asymmetric, especially for the high-frequency mode. Curve fitting by the $U(x) = \kappa x^2 + \beta x^3$ polynomials gives the values of $\beta_1 = 0.427 \times 10^3$ eV/Å^3 and $\beta_2 = -6.22 \times 10^3$ eV/Å^3 for the anharmonicity parameters of the low-frequency and high-frequency modes, respectively.

Fermi resonance in fullerene C_{60}. Measurements [5] of the $A_g(2)$ line shape in the Raman spectra of isotopically pure $^{12}C_{60}$ and $^{13}C_{60}$ fullerenes at temperature 2 K revealed the doublet line structure with splitting of 2 cm^{-1} and peak intensities differing by a factor of 10 in

both cases. Inasmuch as the measured frequency of the $A_g(2)$ vibration is approximately three times as great as the $A_g(1)$ frequency, while the computational results (Fig. 3) indicate that the totally symmetric vibrations are anharmonic, one can assume that there is a Fermi resonance between the $A_g(2)$ fundamental and the second overtone $3A_g(1)$. Using the experimentally observed intensity ratio of the doublet components and the line splitting value and applying the first-order perturbation theory for two closely spaced levels, one arrives at the value of 0.55 ± 0.08 cm^{-1} for the coupling constant of the interacting modes. If one assumes that the suggested line-splitting mechanism is valid, then this experimental value of coupling constant can be used to improve the existing models of the C_{60} molecule.

REFERENCES

1. H. A. Jahn and E. Teller, Proc. R. Soc. London, Ser. A **161**, 220 (1937).
2. E. Fermi, Z. Phys. **71**, 250 (1931).
3. M. P. Lisitsa and A. M. Yaremko, *Fermi Resonance* (Naukova Dumka, Kiev, 1984).
4. M. Lanno, G. A. Baraff, M. Schlüter, and D. Tomanek, Phys. Rev. B **44**, 12106 (1991).
5. P. J. Horoyski, M. L. W. Thewalt, and T. R. Anthony, Phys. Rev. B **54**, 920 (1996).
6. J. J. P. Stewart, MOPAC manual (1993, 7th ed.); J. Comput. Chem. **10**, 209 (1989).
7. A. V. Eletskiĭ and B. M. Smirnov, Usp. Fiz. Nauk **163** (3), 33 (1993) [Phys. Usp. **36**, 202 (1993)].
8. F. Leclercq, P. Damay, M. Foukani, *et al.*, Phys. Rev. B **48**, 2748 (1993).
9. V. V. Dikiĭ and G. Ya. Kabo, Usp. Khim. **69**, 107 (2000).
10. E. S. Stanton and M. D. Newton, J. Phys. Chem. **92**, 2141 (1988).

Translated by V. Sakun

JETP Letters, Vol. 71, No. 12, 2000, pp. 511–515. Translated from Pis'ma v Zhurnal Éksperimental'noĭ i Teoreticheskoĭ Fiziki, Vol. 71, No. 12, 2000, pp. 745–751.

Population Inversion and IR Amplification Induced by Intersubband Electron Transitions and Resonant Auger Processes in Quantum Wells

L. E. Vorob'ev

St. Petersburg State Technical University, ul. Politekhnicheskaya 29, St. Petersburg, 195251 Russia
e-mail: lvor@twonet.stu.neva.ru

Received April 11, 2000; in final form, May 24, 2000

A mechanism for electron population inversion and mid-IR amplification is proposed for the case of the current or optical injection of electron–hole pairs into the undoped region of a heterojunction with quantum wells. The presence of an upper long-lived size-quantization level and resonant Auger recombination in the well are crucial features of the mechanism. A long electron lifetime at the upper level or a relatively low probability of electron scattering to the other subbands is achieved by choosing the shape of the well and its parameters in such a way as to provide weak overlap between the upper level and two lower level electronic wave functions. Resonant Auger recombination plays a positive role. It stabilizes the electron and hole concentrations at lower levels and makes a substantial contribution to the excitation of the upper electronic level and the population inversion. The degree of population inversion and the gain coefficient are estimated. © *2000 MAIK "Nauka/Interperiodica".*

PACS numbers: 73.61.Ey; 78.66.-w

1. INTRODUCTION

Over a period of about last ten years, a search has been carried out for the methods of creating intraband (within the conduction or valence band) population inversion for charge carriers in quantum wells (QWs). This is dictated by the need for fabricating mid-IR lasers (λ = 5–20 μm) on the intraband (intersubband) optical electron (and hole) transitions. The use of standard injection lasers (including QW lasers) on the interband radiative electron and hole transitions hampers progress in this field, primarily because the probability of radiationless electron–hole Auger recombination increases with decreasing energy gap E_g of a semiconductor. The negative effect of Auger recombination can be overcome by passing to the unipolar systems with QWs. In these systems, the electron (or hole) population inversion has an intraband (intersubband) character, because it is created by passing only the electron (hole) current or by intraband optical pumping. Among numerous ideas for creating population inversion and generating stimulated emission, only two of them have been experimentally implemented so far. This is Kazarinov and Suris' idea about the appearance of the intraband interlevel population inversion in a QW system upon transverse electron transport in an electric field [1] and the idea of creating intersubband population inversion in an asymmetric three-level QW by intraband (intersubband) optical pumping [2]. The first idea was modified and implemented in the so-called quantum cascade laser (QCL) [3, 4], and the second idea was implemented in a unipolar fountain laser [5, 6]. The QCL design is rather complicated, and the threshold current density is as high as J_{th} = 10 kA/cm^2 and over at liquid nitrogen temperature. The ways of reducing the threshold current were suggested in the theoretical works [7–9] (they amounted to determining the ways of reducing the probability of intersubband electron scattering involving QW-confined optical phonons). However, from the viewpoint of the technology of growing structures containing many identical QW systems, such a laser is also not simple in design.

The necessity of using powerful intraband optical pumping by mid-IR radiation (at about 10 μm) in the range close to the fountain laser wavelength (approximately 15 μm) narrows the field of application for the latter.

In [10], an idea was suggested (and more recently realized [11]) for fabricating a new type of promising injectionless IR laser—an interband cascade laser on Sb-containing type II heterojunctions. As distinct from QCL, in an instrument of this type, the transverse current (along the axis of structure growth) induces optical transitions between the size-quantization levels of electrons in the conduction band and holes in the valence band. In this case, the upper level electron lifetime caused by the probability of emitting an optical phonon in the course of intraband (intersubband) electron transitions is 2–3 orders of magnitude longer than in QCL. Accordingly, the threshold current is appreciably lower (J_{th} = 0.3 kA/cm^2 at T = 80 K) than in QCL. The structure design and growth technology are also complex,

0021-3640/00/7112-0511$20.00

while the lasing wavelength does not as yet exceed 4 μm.

In this work, a new mechanism is proposed for creating intraband (intersubband) electron population inversion and for the amplification of mid-IR emission upon current or optical electron injection into the undoped region of a heterojunction containing QW. The mechanism involves some of the elements of physical processes occurring in the aforementioned laser types, as well as the specific features of QWs in these lasers. Among these are the injection of electrons and holes, Auger recombination, intersubband cascade charge-carrier transitions, asymmetric QWs with a long-lived upper level, and QWs in the type II heterojunctions. One of the important features of the mechanism is as follows. Although ordinarily playing a negative part, the Auger processes in our case serve an important positive function: at high injection levels, they stabilize the electron and hole concentrations and provide additional excitation to the upper electronic level in the QW. A laser based on this mechanism is simpler in design than are QCL or interband cascade lasers.

Note that, although the system considered below is based on type II heterojunctions (e.g., Sb-containing heterojunctions of the InAsSb/GaSbAs/AlGaAsSb type), a system of the same operating principle can be constructed with type I heterojunctions containing narrow-band superconductors (e.g., InAsSb/InAsP/AlAsSb or GaInAsSb/GaSb/AlGaAsSb).

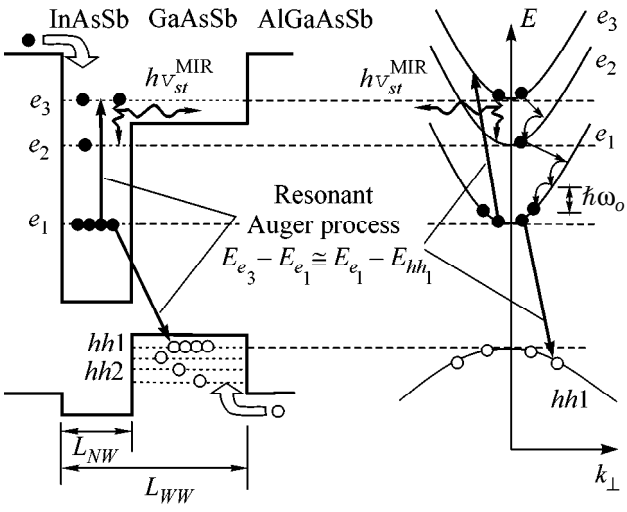

Fig. 1. Scheme of charge-carrier transitions in a QW upon current or optical injection of electrons and holes. The solid lines indicate the following intersubband and intraband radiationless transitions: with emission of optical phonons and the resonant Auger processes. The wavy line indicates the radiative transition between the e_3 and e_2 levels for lasing in the mid-IR (MIR) region. The energy spacings between the e_3 and e_2 and the e_2 and e_1 levels are larger than the optical phonon energy $\hbar\omega_o$. The level e_3 is long-lived. The electron population inversion occurs between the e_3 and e_2 levels (subbands); $k_\perp$ is the in-plane wavevector.

2. MECHANISM OF INTRABAND (INTERSUBBAND) POPULATION INVERSION

Let us consider a heterojunction with electrons confined in an undoped QW in the form of an asymmetric funnel (Fig. 1). Preliminary calculations indicate that the electron and hole QWs with the desired parameters shown in Fig. 1 (see below) can be formed using type II heteropairs, e.g., $In_{1-x}As_xSb/In_{1-y}Ga_ySb_{1-z}As_z$. The well parameters ($L_{NW} \approx 80$ Å and $L_{WW} \approx 300$ Å) and the stoichiometries x, y, and z of the solid solutions are chosen so that the energy spacings $E_{e_3} - E_{e_2}$ and $E_{e_2} - E_{e_1}$ exceed the optical phonon energy $\hbar\omega_o$. In addition, $E_{e_3} - E_{e_2} < E_{e_2} - E_{e_1}$ and the resonance condition $E_{e_3} - E_{e_1} \approx E_{e_1} - E_{hh_1}$ should be approximately fulfilled for the Auger processes.

The mechanism of creating population inversion between the e_3 and e_2 levels can be clarified as follows. Upon the current injection of electrons and holes (in the *p–i–n* structure) or upon the excitation of electron–hole pairs by short-wavelength light with $h\nu > E_{e_3} - E_{hh_3}$, the electrons and holes from the continuum are mainly captured in the upper electron and hole size-quantization levels. The subsequent electron capture in the QW levels and the intersubband transitions can be regarded as scattering with emission of optical phonons. In our system, the interaction with optical phonons dominates. The electron lifetime at the e_3 level is long enough because of the specific well shape (see below). The lifetime at the e_2 level is tangibly shorter. For this reason alone, the population inversion can arise between the e_3 and e_2 levels. The electrons are thrown off the e_1 level due to resonant Auger recombination. Each event of Auger recombination of an electron at the e_1 level and a hole at the h_1 level is accompanied by the excitation of an electron from the e_1 to the e_3 level. Therefore, the e_3 level is additionally populated due to resonant Auger recombination.

If the concentrations of electrons n_1 at the e_1 level and holes p_1 at the hh_1 level are high, then the *e–e* and *e–h* interactions may destroy the inverse population [12]. In order that the n_1 concentration not be too high at high injection levels, an intense Auger recombination is necessary, such that the electron and hole lifetimes at the lower levels are $\tau_A^{-1} = w_A = Bn_1p_1$. If the resonance condition ($E_{e_3} - E_{e_1} \approx E_{e_1} - E_{hh_1}$) is fulfilled in narrow-band materials (in which the difference $E_{e_1} - E_{hh_1}$ is small), the τ_A value may be rather small at the threshold injection levels. Estimations show that, at $E_{e_3} - E_{e_1} \approx 0.3$ eV, τ_A may be of order 10^{-10}–10^{-11} s, while the

quadratic concentration dependence of w_A provides a small change in n_1 as the injection level increases, i.e., in effect, concentration stabilization with an increase in the current or the optical pumping power.

The electron lifetime at the e_2 level at $k_BT < \hbar\omega_o$ is equal to the time $\tau_{21} \approx 0.5$ ps of electron scattering from the e_2 subband to the e_1 subband with emission of an optical phonon. The lifetime at the e_3 level is approximately an order of magnitude longer. This is mainly due to the fact that the e_3 level is genetically associated with a wide well, while the e_2 and e_1 levels originate from the narrow well (Fig. 2). For this reason, the overlap of electron wave functions between the e_3 and e_2 levels and between the e_3 and e_1 levels is weak, while the overlap between the wave functions of the e_2 and e_1 levels is strong (Fig. 2). As a result, the probability of electron transition (scattering) from the subband e_3 to the subband e_2 (w_{32}) or e_1 (w_{31}) with emission of an optical phonon is lower than the scattering probability w_{21} between the subbands e_2 and e_1. Of course, by choosing the funnel-shaped well and reducing the scattering probability w_{32} (and w_{31}), we diminish the matrix element for optical transition $e_3 \longrightarrow e_2$ as well. Nevertheless, it is shown below that the gain coefficient can reach a value that is sufficient for the onset of lasing.

In the above, it is necessary that the phonon-assisted electron capture from continuum by QW mainly occur to the e_3 level. This condition is also fulfilled, because the overlap between the wave functions of electrons in the continuum and at the e_3 level is stronger than the overlap with the wave functions of the e_2 and e_1 states. In addition, the square of the matrix element of the operator of electron interaction with polar optical phonons depends on the phonon in-plane wavevector $q_\perp$ as $|C_q|^2 \sim (q_z^2 + q_\perp^2)^{-1}$. For this reason, the electron transition from the continuum to the lower lying e_2 and e_1 levels is less probable than to the upper e_3 level.

Next we consider the situation where the processes with absorption of optical phonons can be ignored. The probabilities of scattering processes with phonon emission and absorption are proportional to $(N_q + 1)$ and N_q, respectively, where $N_q = (\exp(\hbar\omega_o/k_BT - 1))^{-1}$. Because of this, phonon absorption can be ignored at low temperatures when $(\hbar\omega_o/k_BT > 1$, so that $N_q \ll N_q + 1$. In particular, if $T = 120$ K and $N_q \approx 0.1$, the processes with phonon absorption are insignificant for the QW of interest. As for the absorption of nonequilibrium optical phonons considered in [7] for QCL, the estimates show that, in our case, the nonequilibrium contribution ΔN_q to N_q from the accumulated nonequilibrium phonons does not exceed 0.1 at the threshold current density J_{th}. Hence, the processes with absorption of nonequilibrium phonons can also be ignored. As a result, the electron concentrations at the e_3, e_2, and e_1 levels can be determined from the set of kinetic equations

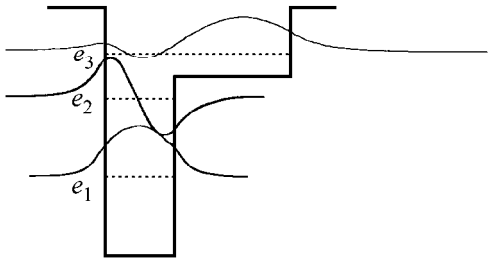

Fig. 2. Electron wave functions in the quantum well (calculation). Weak overlap of the e_3 wave function with the e_2 and e_1 wave functions (compared to the overlap between the wave functions of the e_2 and e_1 levels) provides a long electron lifetime τ_3 at the e_3 level as compared to τ_2.

$$\frac{dn_3}{dt} = A_3\eta\frac{J}{e} - n_3w_{32} - n_3w_{31} + n_1w_A, \quad (1)$$

$$\frac{dn_2}{dt} = A_2\eta\frac{J}{e} + n_3w_{32} - n_2w_{21}, \quad (2)$$

$$\frac{dn_1}{dt} = A_1\eta\frac{J}{e} + n_2w_{21} + n_3w_{31} - 2n_1w_A, \quad (3)$$

where J is the current density; η is the factor responsible for the losses of electrons (holes) moving in the ith layer to the QW; A_i is the coefficient determined by the probability of electron trapping from the continuum to the e_i level in the QW; evidently, $A_1 + A_2 + A_3 = 1$; $w_{ij} = \tau_{ij}^{-1}$ is the probability of electron transition from the subband i to the subband j with emission of optical phonons; and w_A is the probability of Auger recombination $w_A = \tau_A^{-1} = Bn_1p_1$; since $n_1 \approx p_1$, $w_A = Bn_1^2$. The steady-state solution of the set of Eqs. (1)–(3) has the form

$$n_3 - n_2 = \eta\frac{J}{e}\left[(A_1 + A_2 + 2A_3)\frac{w_{21} - w_{32}}{(w_{32} + w_{31})w_{21}} - \frac{A_2}{w_{21}}\right], \quad (4)$$

$$n_1 = \eta\frac{J}{e}w_A^{-1}. \quad (5)$$

In the case of optical pumping, one should substitute $J/e \longrightarrow N_\nu$ in (1)–(5), where N_ν is the photon flux density from the pumping source.

To obtain numerical values of the degree of population inversion $n_3 - n_2$, it is necessary to calculate the scattering w_{ij} and capture A_i probabilities. Let us consider the case $k_BT < \hbar\omega_o$.

The probability of transition from the $E_i(k_{\perp i})$ state to the $E_j(k_{\perp j})$ state ($k_{\perp i}$ is the in-plane wavevector and E_i is

the electron energy in the ith band) with emission of a polar optical phonon of frequency $\hbar\omega_o$ is

$$w_{ij}(k_{\perp i}, k_{\perp j}) = \frac{2\pi}{\hbar}\left|M_{ij}^{PO}\right|^2\delta[E_i(k_{\perp i}) - E_i(k_{\perp j}) - \hbar\omega_o], \quad (6)$$

where M_{ij}^{PO} is the matrix element of the operator of electron interaction with polar optical phonons and the electron energy in the bands i or j is

$$E_{i,j}(k_{\perp i,j}) = E_{i,j} + \hbar^2 k_{\perp i,j}^2/2m_e.$$

The total probability of electron transition from the state with wavevector $k_{\perp i}$ in the ith band to all possible states in the jth band is equal to

$$W_{ij}(k_{\perp i}) = \frac{2\pi}{\hbar}\sum_{k_{\perp j}}\sum_{q_z}|C_q|^2|J_{ji}(q_z)|^2\delta_{q_\perp, k_{\perp i}-k_{\perp j}} \times\delta\left[E_i + \frac{\hbar^2 k_{\perp i}^2}{2m_e} - E_j + \frac{\hbar^2 k_{\perp j}^2}{2me} - \hbar\omega_o\right]. \quad (7)$$

Here, C_q specifies the energy of electron interaction with polar optical phonons:

$$|C_q|^2 = \frac{2\pi e^2\hbar\omega_o}{V(q_z^2 + q_\perp^2)\epsilon^*}, \quad \frac{1}{\epsilon^*} = \frac{1}{\epsilon_\infty} - \frac{1}{\epsilon_0}, \quad (8)$$

where V is the volume; $q_\perp$ is the in-plane phonon wavevector component and q_z is the component along the growth axis; ϵ_∞ and ϵ_0 are the rf and the static permittivities, respectively; and J_{ji} is equal to

$$J_{ji}(q_z) = \int\psi_j^*(z)e^{-iq_z z}\psi_i(z)dz. \quad (9)$$

It follows from (9) that J_{ji} depends on the overlap between the wave functions of the size-quantization levels j and i in the well.

Let us use Eqs. (6)–(9) to estimate the transition probabilities. First of all, $A_1 \gg A_2, A_3$. For w_{ij}, one has $w_{32} = 1.5\times10^{11}$ s^{-1}, $w_{31} = 4.5\times10^{10}$ s^{-1}, and $w_{21} = 2.5\times10^{12}$ s^{-1}. Note that, according to calculations, the probabilities of intraband transitions are much higher than those of the intersubband transitions: $w_{ii}, w_{jj} \gg w_{ij}$. Thus, the calculations show that the electron lifetime at the e_3 level is longer than at the e_2 level by a factor of approximately 12. The results of our calculations agree with the experimental data on the transmission of light with $h\nu > E_g$ through a structure with funnel-shaped QWs upon interband excitation by picosecond optical pulses [13]. It was established in [13] that the electron lifetime at the e_3 level of the funnel-shaped QWs is longer than at the e_2 level by more than an order of magnitude.

3. GAIN AND LASING IN THE MID-IR REGION

The emission gain can readily be calculated for the intersubband transitions in QW. It is equal (without taking into account the parabolicity of the electron energy spectrum) to

$$\alpha_{32} = \frac{4\pi e^2(n_3 - n_2)\omega_{32}^2 z_{32}^2}{c\sqrt{\epsilon_\infty}L\omega}\frac{\gamma}{\gamma^2 + (\hbar\omega - \hbar\omega_{ij})^2}, \quad (10)$$

where $w_{32} = (E_{e_3} - E_{e_2})/\hbar$; z_{32} is the matrix element determining the probability of optical transition; L is the QW width; 2γ is the absorption linewidth for the $E_{e_3} \longrightarrow E_{e_2}$ transition; and $n_3 - n_2$ is the degree of population inversion (4).

Let us estimate the threshold current for mid-IR lasing ($\lambda \approx 12$ μm) or the optical pumping threshold power for a system with a waveguide made from the solid solution $Al_xGa_{1-x}As_{1-y}Sb_y$ with the aluminum percentage x gradually increasing from the QW edge to the periphery of the structure. The condition for lasing is well known:

$$\Gamma\alpha_{32} = \frac{1}{l_R}\ln\frac{1}{R} + \alpha_{loss}, \quad (11)$$

where Γ is the optical confinement factor, l_R is the resonator length, R is the coefficient of reflection from each of the mirrors, and α_{loss} is the loss factor. The losses may be caused by the absorption of mid-IR emission by free charge carriers in the QW and resonator and by two-phonon absorption in the lattice of the GaAlAsSb compound in the resonator.

Let us estimate the threshold current or the optical pumping threshold power density for a single QW. For $\sqrt{\epsilon_\infty} = 3.5$, $R = 0.3$, $l_R = 1.5$ mm, $\Gamma = 2\times10^{-3}$, $\alpha_{loss} = 0$, $\omega = \omega_{32}$, $\gamma = 10$ meV, and $\eta = 1$, we find $J_{th} = 2$ kA/cm^2. This value is smaller than for the quantum cascade lasers. For the optical pumping source wavelength $\lambda = 0.5$ μm, the interband ($h\nu > E_g$) optical pumping threshold power density is 4×10^3 W/cm^2. For a laser crystal of size 1.5 mm × 200 μm, the interband optical pumping threshold power is equal to 12 W. The same power can be provided by superconductor lasers.

In [5], the α_{loss} value in a GaAlAs waveguide was estimated at 10 cm^{-1} for $\lambda = 12.5$ μm. The authors assumed that it was due to two-phonon absorption. If we assume that $\alpha_{loss} \approx 10$ cm^{-1} in our case as well, the threshold current density and the pump power would increase by a factor of about 2.3.

Let now use Eq. (5) to estimate the electron concentration at the e_1 level. According to the calculations of G.G. Zegrya (Ioffe Physicotechnical Institute, Russian Academy of Sciences), at $|(E_{e_3} - E_{e_1}) - (E_{e_1} - E_{hh_1})| < k_BT$ (i.e., at a relatively small resonance detuning) one has $w_A = 10^{-12}n_1^2$ s^{-1}, where n_1 is the charge-carrier sur-

face density per 1 cm^2. Then for $\alpha_{loss} = 0$ and $J_{th} = 2$ kA/cm^2, one gets $n_1 = 2.5 \times 10^{11}$ cm^{-2}, while for $\alpha_{loss} = 10$ cm^{-1} and $J_{th} = 4.6$ kA/cm^2, $n_1 = 3 \times 10^{11}$ cm^{-2}. The electron–electron interaction does not destroy the population inversion at this concentration [12]. Note that for a structure with many QWs, the n_1 concentration in each QW may be sizably reduced and the conditions for generation will be more favorable as compared to the case of a single QW. The possibility also exists of reducing the threshold current or the interband optical pumping power upon increasing the resonator length l_R or the reflection coefficient R of the resonator mirrors.

I am grateful to R.A. Suris and G.G. Zegrya for discussions. This work was supported in part by the Russian Foundation for Basic Research, the program of the PTSC of the Ministry of Science and Technology of the Russian Federation, and the INTAS Open Call 1999 (grant no. 1242).

REFERENCES

1. R. F. Kazarinov and R. A. Suris, Fiz. Tekh. Poluprovodn. (Leningrad) **5**, 797 (1971) [Sov. Phys. Semicond. **5**, 707 (1971)]; Fiz. Tekh. Poluprovodn. (Leningrad) **6**, 148 (1972) [Sov. Phys. Semicond. **6**, 120 (1972)].
2. F. H. Julien, A. Sa'ar, J. Wang, *et al.*, Electron. Lett. **31**, 838 (1995).
3. J. Faist, F. Capasso, D. L. Sivco, *et al.*, Science (Washington, D. C.) **264**, 553 (1994).
4. A. Tredicucci, C. Gmachi, F. Capasso, *et al.*, Appl. Phys. Lett. **74** (3), 638 (1999).
5. O. Gauthier-Lafaye, S. Sauvage, P. Boucaud, *et al.*, Appl. Phys. Lett. **70** (24), 3197 (1997).
6. O. Gauthier-Lafaye, F. H. Julien, S. Cabaret, *et al.*, Appl. Phys. Lett. **74** (11), 1537 (1999).
7. V. F. Elesin and Yu. V. Kopaev, Zh. Éksp. Teor. Fiz. **108**, 2186 (1995) [JETP **81**, 1192 (1995)].
8. V. F. Elesin, V. V. Kopaev, Yu. V. Kopaev, *et al.*, Pis'ma Zh. Éksp. Teor. Fiz. **66** (11), 709 (1997) [JETP Lett. **66**, 742 (1997)].
9. Yu. V. Kopaev, Izv. Ross. Akad. Nauk, Ser. Fiz. **64** (2), (2000).
10. R. Q. Yang, Superlattices Microstruct. **17**, 77 (1995).
11. R. Q. Yang, B. H. Yang, D. Zhang, *et al.*, Appl. Phys. Lett. **71** (17), 2409 (1997).
12. P. Kinsler, P. Harrison, and R. W. Kelsall, Phys. Rev. B **58**, 4771 (1998).
13. C. Y. Sung, T. B. Norris, A. Afrali-Kushaa, *et al.*, Appl. Phys. Lett. **68** (4), 435 (1996).

Translated by V. Sakun

JETP Letters, Vol. 71, No. 12, 2000, pp. 516–519. Translated from Pis'ma v Zhurnal Éksperimental'noĭ i Teoreticheskoĭ Fiziki, Vol. 71, No. 12, 2000, pp. 752–757.

Electron Subsystem Superheating as a Cause of Nonlinear Current–Voltage Characteristics of Amorphous InO_x Films

M. V. Golubkov* and G. É. Tsydynzhapov

Institute of Solid-State Physics, Russian Academy of Sciences, Chernogolovka, Moscow region, 142432 Russia

** e-mail: golubkov@newmail.ru*

Received May 24, 2000

Current–voltage characteristics of amorphous InO_x films in the region of the magnetic-field-induced superconductor–insulator transition were examined. The characteristics are shown to be nonlinear above the critical field because of the superheating of charge carriers in the lattice. There is some evidence that this mechanism is operative below the transition point as well. In this case, the heating fully masks the effect of an electric field in the vicinity of the superconductor–insulator transition. © *2000 MAIK "Nauka/Interperiodica".*

PACS numbers: 71.30.+h; 73.50.Fq; 74.76.Db

In spite of extensive experimental material on the problem of the magnetic-field-induced superconductor–insulator transition [1– 4], only a few works touched on the effect of an electric field on the properties of a system near the transition point [2, 3, 5]. Interest in studying nonlinear current–voltage characteristics is caused by the possibility of determining the critical indices [2, 6] which reflect the fundamental properties of the transition. However, these investigations face problems associated with the necessity of avoiding superheating of a system by an electric current.

The behavior of a system near the superconductor–insulator transition in a magnetic field is described by the single-parameter scaling theory [6]. The correlation length ξ is the key parameter of this theory. It diverges near the transition point following the $\xi \propto \delta^{-\nu}$ law, where $\delta = B - B_c$ is the distance from the transition point B_c and ν is the critical index. The correlation length is related to the characteristic energy scale as $\Omega \propto \xi^{-z}$, where z is the dynamical index. The length scales larger than $l_T \propto T^{-1/z}$ and corresponding to energies lower than T are excluded from consideration at nonzero temperatures T. Similarly, the length $l_E \propto E^{-1/(z+1)}$ corresponding to the energy $el_E E$ is associated with electric field E. Resistance is a universal function of l_T/ξ at $l_T \ll l_E$ ($E \longrightarrow 0$) [8]:

$$R(T) = R_c r_1(\delta/T^{1/z\nu}), \tag{1}$$

or of l_E/ξ at $l_T \gg l_E$ ($T \longrightarrow 0$):

$$E/I = R_c r_2(\delta/E^{1/(z+1)\nu}). \tag{2}$$

The transition from Eq. (1) to Eq. (2) occurs at a temperature below $T_0 \propto E^{z/(z+1)}$.

Apart from Eq. (2), the nonlinearity of the current–voltage characteristics may be due to electron heating by Joule heat $\propto E^2$. The energy scattered by the electric field is dissipated into phonons. The energy flux Q to the phonons is a power function of the electron temperature T_e, $Q \propto T_e^{\theta}$, with the exponent θ dependent on a particular mechanism of electron-phonon interaction [9]. The resulting steady-state electron temperature is determined by the balance of energy fluxes $T_e \propto E^{2/\theta}$.

Comparing expressions for T_0 and T_e with each other, one can see that nonlinear effects without strong superheating can occur only if [7]

$$z/(z+1) > 2/\theta. \tag{3}$$

We undertook investigation of the current–voltage characteristics (CVC) in the vicinity of the magnetic-field-induced superconductor–insulator transition in an amorphous InO_x film. (The properties of the transition in this film are discussed in detail in [4]). The studies were performed for four states with different carrier concentrations, which were varied by changing the oxygen content during the course of low-temperature ($\leq$100°C) vacuum annealing.

An InO_x film was deposited onto a glass substrate and had the shape of a rectangle. The separation between the potential contacts coincided with the film width (6 mm), and the film thickness was 200 Å. The resistance was measured as a function of the magnetic field at a constant temperature by the standard four-probe scheme using a lock-in amplifier at a frequency of 23 Hz. The CVC (the dU/dI derivative as a function of the magnitude of dc current I) was recorded using the modulation technique at fixed temperature and field. The amplitude of current modulation was 10 nA. Most CVC measurements were performed at a temperature of 32 mK.

For different states, we used different magnetic-field orientations about the film surface. In one case, the field

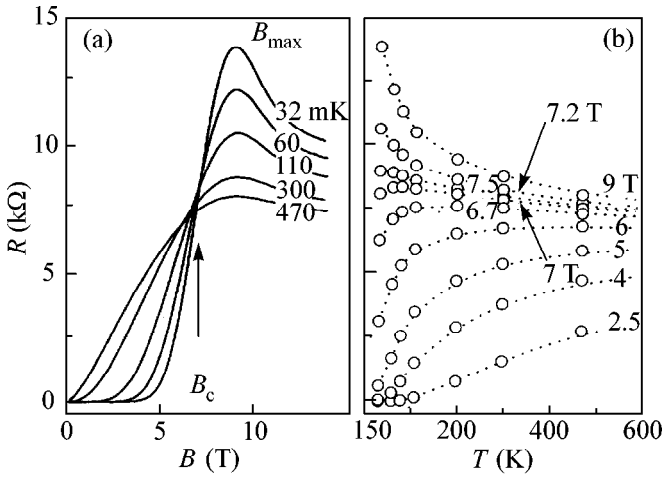

Fig. 1. (a) Resistance of the InO_x film vs. magnetic field at different temperatures; state 1. (b) The same data as functions of temperature.

was perpendicular to the plane; and in three cases, it was parallel (perpendicular to the current). It was found that the character of the CVC and its evolution with magnetic field did not depend on the field direction; nor did the overall pattern of the superconductor–insulator transition [10]. In this work, we report the data for two states with approximately identical concentrations: state 1 in the perpendicular magnetic field and state 2 in the parallel field.

The resistance isotherms $R(B)$ shown in Fig. 1a for one of the states demonstrate the magnetic-field-induced superconductor– insulator transition in the perpendicular field. The transition critical field B_c separating the dielectric and superconducting regions is indicated by the arrow. The field B_{max} corresponding to the maximum in the low-temperature $R(B)$ curves is also indicated. The same data plotted in Fig. 1b as functions of temperature demonstrate the classical superconductor–insulator transition "fan."

The solid lines in Figs. 2a and 2b correspond to the sets of dU/dI dependences for the same state at a temperature of 32 mK in different magnetic fields (in Figs. 2a and 2b, the fields are lower and higher than B_{max}, respectively). The run of the curves has the same features for all states studied. In weak magnetic fields, the CVC have the "Josephson" form with a positive derivative. In the range of strong currents, the behavior of the CVC near B_c is qualitatively different: the derivative becomes negative, and the curves show a "tunnel" character. The peak amplitude increases with an increase in the field below B_{max} and decreases upon its further increase (see. Fig. 2b).

A small sharp minimum at $I = 0$ near B_c (curve 7 T, Fig. 2a) is not reproduced from state to state: its magni-

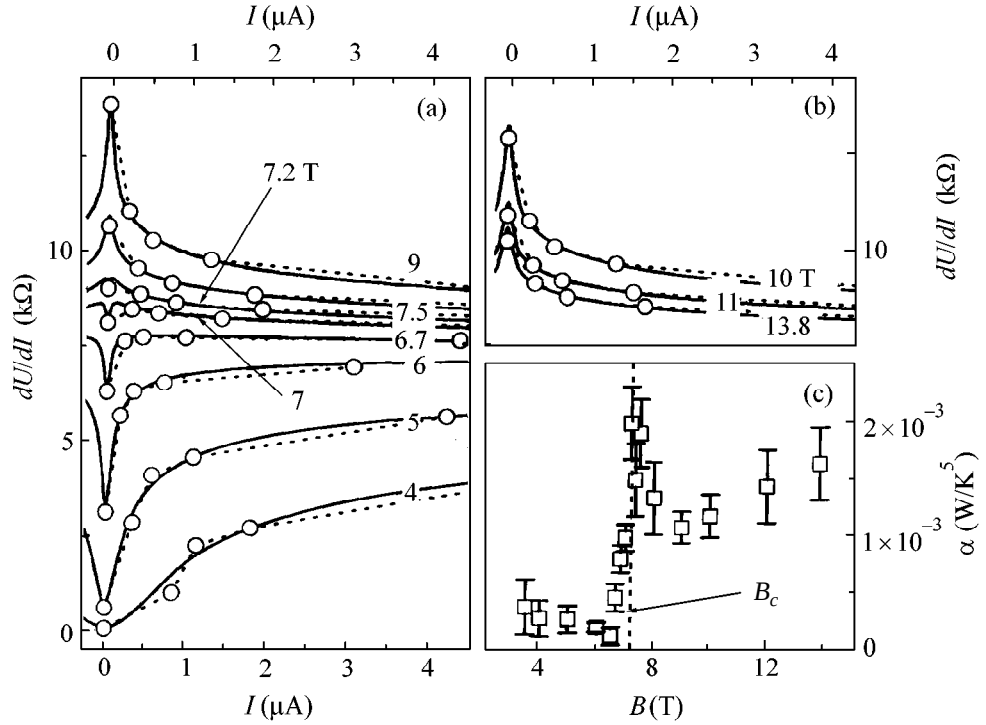

Fig. 2. (a) Comparison of the (solid lines) measured and (dots) calculated dU/dI values for $B < B_{max}$; state 1; $T = 32$ mK. (b) The same for $B \geq B_{max}$. (c) Fitting parameter α.

tude and sign change (i.e., a maximum may appear instead of the minimum). A narrow maximum in the vicinity of the CVC zero was observed for the granulated In/InO_x films in [5], where it was assigned to the Coulomb blockade. The presence of the negative feature in our case rules out an analogous explanation, so that its origin remains to be clarified. It is conceivable that this feature is caused by the macroscopic inhomogeneity of B_c in a small area of the film.

The $R(T)$ curves shown in Fig. 1b and the $dU/dI(I)$ curves in Fig. 2 are, in a sense, similar: the ranges of resistances in the same magnetic field are close, the signs of the derivatives coincide, and the curves show the same nonmonotonic behavior (curves 7 and 7.2 T). It turns out that, after the $T \propto I^{0.4}$ transformation, these curves superpose well on one another. Such a power law relationship may follow from Eqs. (1) and (2) with exponent $z/(z + 1)$. However, it is always greater than 0.5, because $z \geq 1$ [7]. On the other hand, a value of 0.4 may well correspond to superheating with $\theta = 5$.

A value of $\theta = 5$ is observed for metals and superconductors when the deformation interaction of electrons with acoustic phonons dominates at low temperatures. At a nonzero lattice temperature, the heat flux from electrons to phonons in a unit volume of the sample is [9]

$$Q = \alpha(T_e^5 - T_{ph}^5), \quad T_e \ll (8ms^2\varepsilon_F)^{1/2}, \tag{4}$$

where T_{ph} is the phonon (lattice) temperature, α is the coefficient of proportionality, s is the sound velocity, m is the electron mass, and ε_F is the Fermi energy. The law (4) is valid at high fields (in the absence of superconductivity), because, in our experiments, $\varepsilon_F \approx 600$ K, $s \sim 3 \times 10^3$ m/s, and $T_e \lesssim 1$ K.

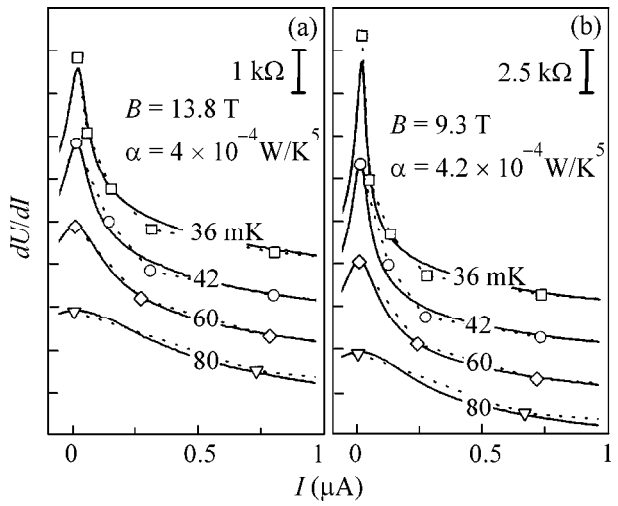

Fig. 3. Comparison of the (solid lines) measured and (dots) calculated dU/dI values at different T; state 2. (a) $B = 13.8$ T, $\alpha = 4 \times 10^{-4}$ W/K^5. The curves are shifted along the vertical line by 1 kΩ relative to each other. (b) $B = B_{max} = 9.3$ T, $\alpha = 4.2 \times 10^{-4}$ W/K^5. The curves are shifted along the vertical line by 2.5 kΩ relative to each other.

If the nonlinear behavior of the CVC is due to the heating of the electron subsystem alone, the dependence of voltage U on the current I and the bath temperature T has the form

$$U(I, T) = IR(T_e), \tag{5}$$

where the electron temperature T_e depends on the current and the external temperature and is determined by the balance between the Joule heat $I^2R(T_e)$ released in a sample and the energy flux Q from electrons to phonons. The lattice temperature T_{ph} is assumed to coincide with the helium bath temperature T, because the sample is immersed into liquid helium and the heat resistance at the interface is negligible under these conditions ($T \geq 32$ mK). Hence it follows that the relation between the current and electron temperature is

$$I = \alpha^{1/2}\left(\frac{T_e^5 - T^5}{R(T_e)}\right)^{1/2}. \tag{6}$$

The total derivative dU/dI measured upon heating the electron subsystem includes, apart from the differential resistance $\partial U/\partial I$, an additional term $(\partial U/\partial T)(\partial T/\partial I)$ associated with heating of the system by the modulation current. From Eq. (5) one has

$$\frac{dU}{dI} = R(T_e) + I\frac{dR(T_e)}{dT}\frac{\partial T_e}{\partial I}. \tag{7}$$

Making use of the experimentally measured $R(T)$ functions (Fig. 1b) and the $T_e(I)$ values implicitly specified by Eq. (6), one can obtain from Eq. (7) the $dU/dI(I)$ dependences in the form $f_{B,T}(\alpha^{-1/2}I)$ incorporating a single fitting parameter α. The calculated $dU/dI(I)$ values are shown in Figs. 2a and 2b by points, and the adjusted α values are given in Fig. 2c. At high fields up to B_c, the agreement between computation and experiment is excellent. On further field decrease, the agreement is noticeably impaired, as is reflected, among other things, in the increased error of determining α.

As the field decreases below B_c the α value turns virtually to zero, indicating that the heat transfer to the lattice is inefficient and model (4) no longer applies.

Additional evidence for the role of superheating is provided by the measurements of dU/dI for state 2 at different temperatures of the helium bath. As shown in Fig. 3, after the α value was derived from the lowest temperature curve, the substitution of new T values in Eq. (6) gives a good agreement with the experimental data, and all curves at $T > 32$ mK are described without a single fitting parameter.

At the highest magnetic fields above B_{max}, the applicability of Eq. (4) is beyond question. For this reason,

the agreement between the calculation and the experiment leads to an intrinsically consistent picture, in which the CVC nonlinearity is due solely to superheating of the electron subsystem.

At lower fields (between B_{max} and B_c), the state of the electron subsystem is unclear, so that Eq. (4) cannot be theoretically substantiated with confidence. However, because of the excellent agreement between the calculation and the experiment, one can assume that the transport and the heat transfer to phonons are dominated by normal electrons whose density of states is finite near the Fermi surface [11].

Therefore, superheating is the main cause for the CVC nonlinearity in the vicinity of the transition as well. Since the observed θ value is equal to 5, one cannot observe, according to Eq. (3), the direct influence (2) of an electric field on the superconductor–insulator transition. Indeed, our attempts at scaling CVC by this formula have not been successful.

At fields below B_c, when the film resistance becomes lower than in the normal state, the role of Cooper pairs in transport cannot be ignored. It is thus not surprising that the agreement between the calculation based on Eq. (4) and the experimental curves fades away. Nevertheless, we suppose that the behavior of the electron subsystem upon applying an electric field in this region is also governed by superheating. At least, we do not know of any data that contradict this hypothesis.

In summary, we have shown that the effect of an electric field on InO_x films at low temperatures amounts to the superheating of electron subsystem with respect to phonons. We revealed that the heat transfer from electrons to phonons is proportional to the fifth power of temperature and corresponds to the deformation interaction of electrons with acoustic phonons.

This conclusion means, in particular, that the direct effect of an electric field on the superconductor–insulator transition in a magnetic field cannot be observed for the object studied.

We are grateful to V.F. Gantmakher, V.T. Dolgopolov, S.I. Dorozhkin, and M.S. Skvortsov for valuable discussions and remarks. This work was supported by the Russian Foundation for Basic Research (project no. 99-02-16117), the Russian Foundation for Basic Research-PICS (project no. 98-02-22037), and the program "Statistical Physics" of the Ministry of Sciences of the Russian Federation.

REFERENCES

1. A. F. Hebard and M. A. Paalanen, Phys. Rev. Lett. **65**, 927 (1990); S. Okuma, T. Terashima, and N. Kokubo, Solid State Commun. **106**, 529 (1998).
2. A. Yadzani and A. Kapitulnik, Phys. Rev. Lett. **74**, 3037 (1995).
3. N. Marković, C. Christiansen, A. M. Mack, *et al.*, Phys. Rev. Lett. **60**, 4320 (1999).
4. V. F. Gantmakher, M. V. Golubkov, V. T. Dolgopolov, *et al.*, Pis'ma Zh. Éksp. Teor. Fiz. **71**, 231 (2000) [JETP Lett. **71**, 160 (2000)].
5. J. J. Kim, J. Kim, and H.-L. Lee, Phys. Rev. B **46**, 11709 (1992).
6. M. P. A. Fisher, Phys. Rev. Lett. **65**, 923 (1990).
7. S. L. Sondhi, S. M. Girvin, J. P. Carini, and D. Shahar, Rev. Mod. Phys. **69**, 315 (1997).
8. M. P. A. Fisher, G. Grinstein, and S. M. Girvin, Phys. Rev. Lett. **64**, 587 (1990).
9. V. F. Gantmakher and I. B. Levinson, *Scattering of Charge Carriers in Metals and Superconductors* (Nauka, Moscow, 1984).
10. V. F. Gantmakher, M. V. Golubkov, V. T. Dolgopolov, *et al.*, Ann. Phys. (Leipzig) **8**, SI-73 (1999).
11. V. F. Gantmakher, M. V. Golubkov, V. T. Dolgopolov, *et al.*, Pis'ma Zh. Éksp. Teor. Fiz. **68**, 345 (1998) [JETP Lett. **68**, 363 (1998)].

Translated by V. Sakun